Atmos. Chem. Phys., 17, 2279–2296, 2017
www.atmos-chem-phys.net/17/2279/2017/
doi:10.5194/acp-17-2279-2017

Atmospheric Chemistry and Physics
Open Access
EGU

Observations and model simulations of snow albedo reduction in seasonal snow due to insoluble light-absorbing particles during 2014 Chinese survey

Xin Wang[1], Wei Pu[1], Yong Ren[1], Xuelei Zhang[2], Xueying Zhang[1], Jinsen Shi[1], Hongchun Jin[1], Mingkai Dai[1], and Quanliang Chen[3]

[1]Key Laboratory for Semi-Arid Climate Change of the Ministry of Education, College of Atmospheric Sciences, Lanzhou University, Lanzhou, 730000, China
[2]Key Laboratory of Wetland Ecology and Environment, Northeast Institute of Geography and Agroecology, Chinese Academy of Sciences, Changchun 130102, China
[3]College of Atmospheric Science, Chengdu University of Information Technology, and Plateau Atmospheric and Environment Laboratory of Sichuan Province, Chengdu 610225, China

Correspondence to: Xin Wang (wxin@lzu.edu.cn)

Received: 23 July 2016 – Discussion started: 21 September 2016
Revised: 16 January 2017 – Accepted: 16 January 2017 – Published: 14 February 2017

Abstract. A snow survey was carried out to collect 13 surface snow samples (10 for fresh snow, and 3 for aged snow) and 79 subsurface snow samples in seasonal snow at 13 sites across northeastern China in January 2014. A spectrophotometer combined with chemical analysis was used to quantify snow particulate absorption by insoluble light-absorbing particles (ILAPs, e.g., black carbon, BC; mineral dust, MD; and organic carbon, OC) in snow. Snow albedo was measured using a field spectroradiometer. A new radiative transfer model (Spectral Albedo Model for Dirty Snow, or SAMDS) was then developed to simulate the spectral albedo of snow based on the asymptotic radiative transfer theory. A comparison between SAMDS and an existing model – the Snow, Ice, and Aerosol Radiation (SNICAR) – indicates good agreements in the model-simulated spectral albedos of pure snow. However, the SNICAR model values tended to be slightly lower than those of SAMDS when BC and MD were considered. Given the measured BC, MD, and OC mixing ratios of 100–5000, 2000–6000, and 1000–30 000 ng g^{-1}, respectively, in surface snow across northeastern China, the SAMDS model produced a snow albedo in the range of 0.95–0.75 for fresh snow at 550 nm, with a snow grain optical effective radius (R_{eff}) of 100 µm. The snow albedo reduction due to spherical snow grains assumed to be aged snow is larger than fresh snow such as fractal snow grains and hexagonal plate or column snow grains associated with the increased BC in snow. For typical BC mixing ratios of 100 ng g^{-1} in remote areas and 3000 ng g^{-1} in heavy industrial areas across northern China, the snow albedo for internal mixing of BC and snow is lower by 0.005 and 0.036 than that of external mixing for hexagonal plate or column snow grains with R_{eff} of 100 µm. These results also show that the simulated snow albedos by both SAMDS and SNICAR agree well with the observed values at low ILAP mixing ratios but tend to be higher than surface observations at high ILAP mixing ratios.

1 Introduction

Mineral dust (MD), black carbon (BC), and organic carbon (OC) are three main types of insoluble light-absorbing particles (ILAPs) that play key roles in regional and global climate (Bond et al., 2013; Dang and Hegg, 2014; Hansen et al., 2005; IPCC, 2013; Li et al., 2016; McConnell et al., 2007; Pu et al., 2015). ILAPs deposited on snow have been found to shorten the snow cover season by decreasing the snow albedo and accelerating snow melt (Brandt et al., 2011; Flanner et al., 2007, 2009; Hadley and Kirchstetter, 2012). The Takla Makan and Gobi deserts and several other deserts are

well known dust sources across northern China. MD particles produced in these deserts can be lifted up in the atmosphere and transported to the downwelling regions (Che et al., 2011, 2013; Chen et al., 2013; Huang et al., 2008; Jaffe et al., 1999; X. Wang et al., 2008, 2010; Zhang et al., 2003). Carbonaceous aerosols, such as BC and OC, generated from the incomplete combustion of fossil fuels and from biomass burning, are also major anthropogenic pollutants. A mixing ratio of 10 ng g^{-1} of soot in snow can reduce snow albedo by 1 % (Warren and Wiscombe, 1980). 150 ng g^{-1} of BC embedded in sea ice can reduce ice albedo by up to 30 % (Light et al., 1998). At 500 nm 1 ng g^{-1} of BC has approximately the same effect as 50 ng g^{-1} of dust on the albedo of snow and ice (Warren, 1982). Yasunari et al. (2015) suggested that the existence of snow darkening effect in the earth system associated with ILAPs contributes significantly to enhanced surface warming over continents in northern hemispheric midlatitudes during boreal spring, raising the surface skin temperature by approximately 3–6 K near the snow line. Modeling soot in snow as an "external mixture" (impure particles separated from ice particles), if it is actually located inside the ice grains as an "internal mixture", may underestimate its true effect on albedo reduction by 50 % (Warren and Wiscombe, 1985). Assuming internal rather than external mixing of BC in snow increased BC absorption coefficient by a factor of 2 and gained better agreement with empirical data (Cappa et al., 2012; Hansen and Nazarenko, 2004). Increasing the size of snow grains could decrease snow albedo and amplify the radiative perturbation of BC (Hadley and Kirchstetter, 2012). For a snow grain optical effective radius (R_{eff}) of 100 µm, the albedo reduction caused by 100 ng g^{-1} of BC is 0.019 for spherical snow grains but only 0.012 for equidimensional nonspherical snow grains (Dang et al., 2016). BC coated with non-absorbing particles absorbs more strongly than the same amount of BC in an uncoated particle, but the magnitude of this absorption enhancement is yet to be quantified (Fierce et al., 2016). A modeling study suggested that BC–snow internal mixing increases the albedo forcing by 40–60 % compared with external mixing, and coated BC increases the forcing by 30–50 % compared with uncoated BC aggregates, whereas Koch snowflakes reduce the forcing by 20–40 % relative to spherical snow grains (He et al., 2014).

Although MD is a less efficient absorber than BC and OC, field campaigns on collecting seasonal snow samples across northern China and the Himalayas have shown high MD loadings (Guan et al., 2015; Kang et al., 2016; Wang et al., 2012, 2013a). In some regions, especially areas with thin and patchy snow cover and mountainous regions, soil dust significantly decreases the snow albedo, exceeding the influence of BC. However, models did not capture these potential large sources of local dust in snowpack and may overestimate BC forcing processes (Painter et al., 2007, 2010, 2012). Recently, several seasonal snow collection campaigns were performed across northern China, the Himalayas, North America, Greenland and the Arctic (Cong et al., 2015; Dang and Hegg, 2014; Doherty et al., 2010, 2014; Huang et al., 2011; Xu et al., 2009, 2012; Zhao et al., 2014). However, determining the effects of ILAPs on snow albedo reduction continues to be challenging (Huang et al., 2011; Wang et al., 2013a, 2015; Ye et al., 2012; Zhang et al., 2013a).

To date, only a few studies have compared modeled and observed snow albedo reduction due to ILAPs in snow (Dang et al., 2015; Flanner et al., 2007, 2012; Grenfell et al., 1994; Liou et al., 2014; Warren and Wiscombe, 1980). To gain some in-depth knowledge on this topic, a 2014 snow survey was first performed across northeastern China to analyze light absorption of ILAPs in seasonal snow, and modeling studies were then conducted to compare snow albedo reduction due to various assumptions of internal–external mixing of BC in snow and different snow grain shapes.

2 Experimental procedures

2.1 Snow field campaign in January 2014

There was less snowfall in January 2014 than in previous years (e.g., 2010), and thus only 92 snow samples (13 surface snow including 10 fresh and 3 aged ones, and 79 subsurface snow samples) at 13 sites were collected during this snow survey. The snow sampling sites in this study were numbered starting at 90 (see Fig. 1 and Table 1) following the chronological order from Wang et al. (2013a) and Ye et al. (2012). Samples at sites 90–93 were collected from grassland and cropland areas in Inner Mongolia. Sites 94–98 and 99–102 were located in the Heilongjiang and Jilin provinces, respectively, which were the most heavily polluted areas in northern China during winter. The snow sampling procedures were similar to those used in the previous survey conducted in 2010 across northern China (Huang et al., 2011). To prevent contamination, the sampling sites were positioned 50 km from cities and at least 1 km upwind of approach roads or railways; the only exception was site 101, which was positioned downwind and close to villages. Two vertical profiles of snow samples ("left" and "right") were collected through the whole depth of the snowpack at all the sites to reduce the possible contamination by artificial effects during the sampling process, and the dusty or polluted layers were separately collected during the sampling process. All of the datasets in seasonal snow listed in Table 1 are average values from the two adjacent snow samples through the whole depth of the snowpack. Snow grain sizes (R_{m}) were measured by visual inspection on millimeter-gridded sheets viewed through a magnifying glass. The snow samples were kept frozen until the filtration process was initiated. In a temporary lab based in a hotel, we quickly melted the snow samples in a microwave, let them settle for 3–5 min, and then filtered the resulting water samples through a 0.4 µm Nuclepore filter to extract particulates.

Table 1. Statistics in seasonal snow variables measured using an ISSW in the study sites. All of the datasets are the average values from the left and right snow samples. The site numbers begin at 90 in this study, which are numbered in chronological order followed by Wang et al. (2013a), and Ye et al. (2012).

Site	Layer	Latitude N	Longitude E	Snow type	Site average snow depth (cm)	Sample depth (cm) Top	Sample depth (cm) Bottom	Temperature (°C) Temperature	Snow density ($g\,cm^{-3}$)	R_m (mm)	C_{BC}^{equiv} ($ng\,g^{-1}$)	C_{BC}^{max} ($ng\,g^{-1}$)	C_{BC}^{est} ($ng\,g^{-1}$)	$f_{non\text{-}BC}^{est}$ (%)	$Å_{tot}$ 450 : 600 nm
90	1	45°02′44″	116°22′45″	Aged	3	0	5	−14	0.38	0.15	860	530	330 (–, 470)	61 (45, 110)	3.8
91	1	50°02′48″	124°22′41″	Fresh	8	0	5	−25	0.23	0.08	250	200	160 (110, 200)	35 (18, 55)	2.1
	2			Aged		5	10	−25	0.18	0.15	–	–	–	–	–
92	1	50°39′07″	122°23′53″	Fresh	14	0	5	−16	0.17	0.08	80	70	50 (30, 70)	34 (15, 60)	2.3
	2			Aged		5	10	−16	0.18	1.25	110	100	80 (50, 100)	29 (11, 55)	2.2
93	1	50°24′50″	124°54′20″	Fresh	8	0	1	–	–	0.07	170	100	70 (40, 90)	53 (39, 73)	2.5
	2			Aged		2	6	−21	0.21	0.175	310	140	100 (50, 130)	68 (59, 85)	2.7
94	1	50°09′05″	125°46′06″	Fresh	8	0	1	−24	–	0.1	1200	400	260 (110, 360)	78 (69, 91)	2.8
95	1	50°54′43″	127°04′50″	Aged	18	0	3	−22	0.23	0.175	280	110	80 (40, 100)	73 (64, 86)	2.6
	2			Aged		3	8	−23	0.18	0.9	230	80	50 (30, 70)	77 (68, 89)	2.7
	3			Aged		8	13	−25	0.27	1	90	50	30 (10, 40)	71 (55, 92)	3.2
	4			Aged		13	18	−25	0.14	1.3	520	310	130 (–, 240)	75 (54, 148)	4.8
96	1	49°14′21″	129°43′13″	Fresh	13	0	5	−22	0.37	0.08	1300	390	240 (20, 330)	83 (76, 99)	3.4
	2			Aged		5	10	−23	0.25	0.6	230	90	50 (10, 70)	81 (69, 98)	3.3
	3			Aged		10	15	−22	0.22	1	370	130	80 (30, 110)	80 (71, 93)	3.0
97	1	47°39′18″	131°13′10″	Aged	20	0	5	−22	0.36	0.2	1000	360	240 (90, 310)	76 (69, 91)	2.8
	2			Aged		5	10	−18	0.27	1.1	160	80	50 (20, 70)	71 (57, 91)	3.0
	3			Aged		10	15	−14	0.32	0.9	30	20	10 (5, 20)	74 (44, 90)	3.1
98	1	45°25′38″	130°58′55″	Fresh	35	0	5	−20	0.22	0.09	2200	2100	1500 (750, 1800)	32 (16, 65)	2.5
	2			Aged		5	10	−23	0.24	0.5	640	350	240 (120, 310)	58 (46, 79)	2.6
	3			Aged		10	15	−15	0.24	0.75		60	20 (10, 50)	74 (52, 90)	3.1
	4			Aged		15	20	−14	0.26	0.75	60	40	20 (10, 30)	75 (48, 89)	3.1
	5			Aged		20	25	−13	0.28	1.1	430	260	170 (60, 220)	62 (49, 86)	2.8
	6			Aged		25	30	−11	0.29	1.3	350	170	110 (70, 150)	68 (58, 81)	2.5
	7			Aged		30	35	–	0.33	1.3	290	120	70 (40, 100)	75 (65, 87)	2.6
99	1	43°36′10″	125°42′04″	Fresh	13	0	5	−2	0.18	0.085	1500	920	640 (240, 820)	54 (40, 84)	2.8
	2			Aged		5	12	−3	0.23	1.1	5800	3800	2900 (1500, 3600)	51 (39, 74)	2.5
	3			Aged		12	18	−4	0.28	1.1	2800	1400	1100 (630, 1300)	62 (53, 77)	2.3
	4			Aged		18	24	−4	0.28	0.7	2000	1500	1100 (540, 1400)	46 (32, 73)	2.6
100	1	43°30′45″	127°15′34″	Fresh	18	0	2.5	–	0.14	0.075	1700	700	510 (250, 650)	71 (63, 86)	2.6
	2			Aged		2.5	4	−2	0.18	0.25	4100	2900	1700 (–, 2400)	58 (43, 103)	3.6
	3			Aged		4	9	−2	0.23	0.9	1100	560	410 (210, 530)	60 (49, 80)	2.6
	4			Aged		9	15	−3	0.24	0.8	1600	730	540 (270, 690)	66 (57, 83)	2.6
101	1	43°47′25″	125°46′08″	Fresh	22	0	5	−19	0.24	0.07	5600	5100	3700 (1300, 4600)	35 (18, 76)	2.9
	2			Aged		5	10	−17	0.24	0.9	4300	3800	2600 (880, 3300)	40 (24, 79)	2.9
	3			Aged		10	15	−15	0.23	1.1	660	390	310 (210, 390)	46 (33, 63)	2.1
	4			Aged		15	20	−14	0.28	1.3	300	250	190 (110, 240)	39 (21, 67)	2.5
102	1	42°12′34″	126°37′50″	Fresh	46	0	3	−8	0.13	0.07	2100	1700	1400 (810, 1800)	37 (19, 61)	2.3
	2			Aged		3	8	−8	0.26	0.1	590	380	280 (150, 370)	53 (37, 75)	2.6
	3			Aged		8	13	−8	0.24	0.3	2500	2100	1600 (430, 2100)	35 (15, 81)	3.1

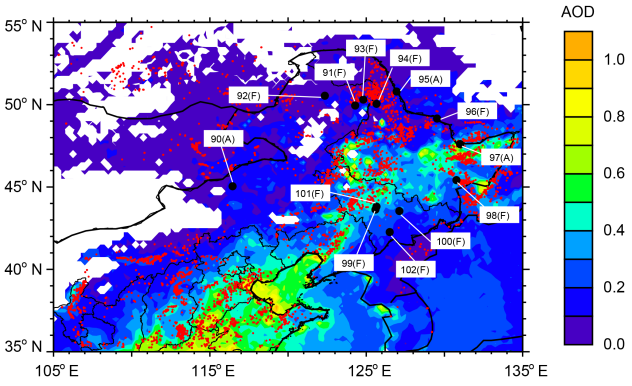

Figure 1. Spatial distribution of the averaged AOD retrieved from Aqua-MODIS over northern China from October 2013 to January 2014. The red dots are MODIS active fire locations, and the black dots are the sampling locations. The site numbers begin at 90 in this study, which are numbered in chronological order followed by Wang et al. (2013a) and Ye et al. (2012). "A" and "F" refer to aged snow and fresh snow, respectively.

2.2 Chemical speciation

Major water-soluble ions and trace elements in surface snow samples during this snow survey have already been investigated by Wang et al. (2015). However, the importance of ILAPs in seasonal snow during this survey has not been discussed yet, which will be addressed below. Briefly, major ions (SO_4^{2-}, NO_3^-, Cl^-, Na^+, K^+, and NH_4^+) were analyzed with an ion chromatograph (Dionex, Sunnyvale, CA), and trace elements of Fe and Al were measured by inductively coupled plasma mass spectrometry (ICP-MS). These analytical procedures have been described elsewhere (Yesubabu et al., 2014). In this paper, the major ions are used to retrieve the sea salt and bio-smoke potassium ($K^+_{Biosmoke}$). Previous studies have revealed considerable variations in iron (Fe) of 2–5 % in dust (Lafon et al., 2006), although Al is more stable than Fe in the earth's crust. Hence, we retrieved the mass concentration of MD via the Al concentration, assuming a fraction of 7 % in MD (Arhami et al., 2006; Lorenz et al., 2006; Zhang et al., 2003). Sea salt was estimated following the method presented in Pio et al. (2007):

$$\text{Seasalt} = Na^+_{Ss} + Cl^- + 0.12Na^+_{Ss} + 0.038Na^+_{Ss} + 0.038Na^+_{Ss} + 0.25Na^+_{Ss}, \quad (1)$$

where subscript Ss means sea salt sources, and Na_{Ss} was calculated using the following formula (Hsu et al., 2009):

$$Na_{Ss} = Na_{Total} - Al \times (Na/Al)_{Crust}. \quad (2)$$

Following Hsu et al. (2009), the contribution of $K^+_{Biosmoke}$ was determined using the following equations:

Table 1. Continued.

Site	Layer	Latitude N	Longitude E	Snow type	Site average snow depth (cm)	Sample depth (cm) Top	Sample depth (cm) Bottom	Temperature	Temperature (°C)	Snow density (g cm^{-3})	R_m (mm)	C^{equiv}_{BC} (ng g^{-1})	C^{max}_{BC} (ng g^{-1})	C^{est}_{BC} (ng g^{-1})	$f^{est}_{non\text{-}BC}$ (%)	$\mathring{A}_{tot}$ 450 : 600 nm
4				Aged		13	18		−8	0.28	0.6	1900	1100	770 (230, 1000)	60 (48, 88)	3.0
5				Aged		18	23		−7	0.32	1	1100	630	450 (200, 590)	60 (47, 82)	2.7
6				Aged		23	28		−6	0.27	1.2	1500	1300	900 (300, 1200)	38 (21, 80)	2.9
7				Aged		28	33		−5	0.26	1.2	860	490	340 (130, 460)	66 (53, 87)	2.9
8				Aged		33	38		−5	0.3	1	430	200	110 (30, 160)	74 (61, 95)	3.2
9				Aged		38	43		−4	0.29	0.8	520	250	160 (70, 220)	71 (58, 87)	2.8

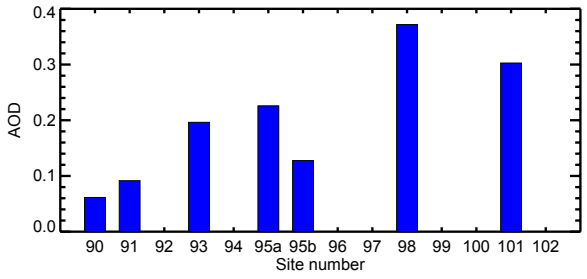

Figure 2. The variation in AOD at 500 nm at different sites measured using a Microtops Π Sunphotometer over northeastern China in January 2014.

$$K^{+}_{Biosmoke} = K_{Total} - K_{Dust} - K_{Ss}, \quad (3)$$

$$K_{Dust} = Al \times (K/Al)_{Crust}, \quad (4)$$

$$Na_{Ss} = Na_{Total} - Al \times (Na/Al)_{Crust}, \quad (5)$$

$$K_{Ss} = Na_{Ss} \times 0.038, \quad (6)$$

where $K^{+}_{Biosmoke}$, K_{Dust}, and K_{Ss} refer to bio-smoke potassium, dust-derived potassium, and sea-salt-derived potassium, respectively. Equations (4), (5), and (6) were derived from Hsu et al. (2009) and Pio et al. (2007).

2.3 Spectrophotometric analysis

Recent studies indicated that the light absorption by MD should be more sensitive to the presence of strongly absorbing iron oxides such as hematite and goethite than to other minerals (Alfaro et al., 2004; Sokolik and Toon, 1999). Thus, it is now possible to assess the absorption properties of MD by using iron oxide content (Bond et al., 1999). In this study, the iron in seasonal snow is assumed to originate from MD during this survey, following the procedures performed by Wang et al. (2013a). We measured the mixing ratios of BC and OC using an integrating sphere/integrating sandwich spectrophotometer (ISSW), which was first described by Grenfell et al. (2011) and used by Doherty et al. (2010, 2014) and Wang et al. (2013a). The equivalent BC (C^{equiv}_{BC}), maximum BC (C^{max}_{BC}), estimated BC (C^{est}_{BC}), fraction of light absorption by non-BC ILAPs ($f^{est}_{non\text{-}BC}$), and absorption Ångström exponent of all ILAPs ($Å_{tot}$) were described by Doherty et al. (2010). Previous studies have concluded that ILAPs are primarily derived from BC, OC, and Fe. The mass loadings of BC (L_{BC}) and OC (L_{OC}) were calculated using the following equation:

$$\tau_{tot}(\lambda) = \beta_{BC}(\lambda) \times L_{BC} + \beta_{OC}(\lambda) \times L_{OC} + \beta_{Fe}(\lambda) \times L_{Fe}. \quad (7)$$

Here, $\tau_{tot}(\lambda)$ refers to the measured optical depth. L_{BC} and L_{OC} can be determined from this equation assuming that the mass absorption coefficients (MACs) for BC, OC, and Fe are 6.3, 0.3, and 0.9 $m^2\,g^{-1}$, respectively, at 550 nm and that the absorption Ångström exponents (Å or AAE) for BC, OC, and Fe are 1.1, 6, and 3, respectively (e.g., Eqs. 2 and 3 in Wang et al., 2013a).

2.4 Aerosol optical depth and snow albedo measurements

The Microtops Π Sunphotometer has been widely used to measure aerosol optical depth (AOD) in recent years (More et al., 2013; Porter et al., 2001; Zawadzka et al., 2014) and is recognized as a very useful tool for validating aerosol retrievals from satellite sensors. Ichoku et al. (2002b) and Morys et al. (2001) provided a general description of the Microtops Π Sunphotometer's design, calibration, and performance. To better understand the background weather conditions in the local atmosphere during this snow survey, we used a portable and reliable Microtops Π Sunphotometer at wavelengths of 340, 440, 675, 870, and 936 nm instead of the CE318 sun tracking photometer to measure the surface AOD in this study. AOD measurements were collected in cloud-free conditions between 11:00 and 13:00 (Beijing local time) to prevent the effects of optical distortions due to large solar zenith angles. Then, the Moderate Resolution Imaging Spectroradiometer (MODIS) on the Aqua and Terra satellites was used to retrieve the AOD and fire spot datasets (Kaufman et al., 1997; Zhang et al., 2013b; Zhao et al., 2014). The retrieved MODIS AOD is reliable and accurate when applied to three visible channels over vegetated land and ocean surfaces (Chu et al., 2002; Ichoku et al., 2002a; Remer et al., 2002). Fire locations are based on data provided by the MODIS Fire Information for Resource Management System (FIRMS) system from October 2013 to January 2014. The land-cover types (Figs. 6 and 7) were obtained from the Collection 5.1 MODIS global land-cover type product (MCD12C1) at a 0.05° spatial resolution and included 17 different surface vegetation types (Friedl et al., 2010; Loveland and Belward, 1997).

Snow albedo plays a key role in energy balance and climate in the cryosphere (e.g., Hadley and Kirchstetter, 2012; Liou et al., 2014; Warren and Wiscombe, 1985). Wright et al. (2014) indicated that the spectral albedo measured using an Analytical Spectral Devices Inc. (ASD) spectroradiometer at 350–2200 nm is in agreement with albedo measurements at the Baseline Surface Radiation Network (BSRN). Wuttke et al. (2006a) pointed out that the spectroradiometer instrument is considered as the most capable, rapid, and mobile for conducting spectral albedo measurements during short time periods, especially in very cold regions (e.g., in the Arctic). The major advantage is the more extensive wavelength range, and the cosine error is less than 5 % for solar zenith angles below 85° at a wavelength of 320 nm (Wuttke et al., 2006a, b). In this study, snow albedo measurements were obtained using a HR-1024 field spectroradiometer (SVC, Spectra Vista Corporation, Poughkeepsie, NY, USA). This instrument has a spectral range of 350–2500 nm with resolutions of

3.5 nm (350–1000 nm), 9.5 nm (1000–1850 nm), and 6.5 nm (1850–2500 nm). Normally, the relative position of the spectroradiometer is at a distance of 1 m from the optical element for the active field of view (Carmagnola et al., 2013). A standard "white" reflectance panel with a VIS–SWIR broadband albedo of 0.98 (P_λ) was used to measure the reflectance spectra along with the target. The reflectance spectra of surface snow (R_s) and the standard panel (R_p) were measured at least 10 times. Then, the snow albedo (α) was calculated as follows:

$$\alpha = (R_s/R_p) \times P_\lambda. \quad (8)$$

The nominal field of view (FOV) lens is 8° to enable the instrument to look at different size targets. In order to receive more direct solar radiation, the direction of the instrument was oriented to the sun horizon angles to measure snow albedo. The small size of the fore optics greatly reduces errors associated with instrument self-shadowing. Even when the area viewed by the fore optic is outside the direct shadow of the instrument, the instrument still blocks some of the illumination (either diffuse skylight or light scattered off surrounding objects) that would normally strike the surface under observation for measuring full-sky irradiance throughout the entire 350–2500 nm wavelengths. Further information on the HR-1024 field spectroradiometer used and on the calibration procedure can be found in Wright et al. (2014). The measured solar zenith angles and the other parameters used to simulate snow albedo in this study have been labeled in Fig. 11.

2.5 Model simulations

BC and MD sensitivity effects on the snow albedo simulated by the Snow, Ice, and Aerosol Radiation (SNICAR) model have been validated through recent simulations and field measurements (Flanner et al., 2007, 2009; Qian et al., 2014; Zhao et al., 2014). We used the offline SNICAR model to simulate the reduction in surface snow albedo resulting from ILAP contamination (Flanner et al., 2007), and we compared the results with our spectroradiometer surface measurements. The SNICAR model calculates the snow albedo as the ratio of the upward to downward solar flux at the snow surface. The measured parameters, including the measured snow grain radius (R_m), snow density, snow thickness, solar zenith angle θ, and mixing ratios of BC and MD, were used to run the SNICAR model under clear sky conditions. The visible and near-infrared albedos of the underlying ground were 0.2 and 0.4, respectively, as derived from MODIS remote sensing. The MAC of BC was assumed to be 7.5 $m^2\ g^{-1}$ at 550 nm.

The Spectral Albedo Model for Dirty Snow (SAMDS) based on asymptotic radiative transfer theory was used for calculating spectral snow albedo as a function of the snow grain radius, the mixing ratios of ILAPs (BC, MD, and OC), and MACs of impurities. A detailed description of asymptotic analytical radiative transfer theory for SAMDS can be found in Zhang et al. (2017). Briefly, the surface albedo can be calculated using the following asymptotic approximate analytical solution derived from radiative transfer theory (Kokhanovsk and Zege, 2004; Rozenberg, 1962; Zege et al., 1991):

$$R_d(\lambda) = \exp(-4S(\lambda)\mu(\nu_0)). \quad (9)$$

Here, $R_d(\lambda)$ is the plane albedo, ν_0 is the solar zenith angle, and $\mu(\nu_0)$ refers to the escape function in radiative transfer theory and is parameterized following Kokhanovsky and Zege (2004):

$$\mu(\nu_0) = \frac{3}{7}(1 + 2\cos\nu_0), \quad (10)$$

where λ is the wavelength, $S(\lambda)$ is the similarity parameter, and

$$S(\lambda) = \sqrt{\frac{\sigma_{abs}}{3\sigma_{ext}(1-g)}}. \quad (11)$$

Here, σ_{abs} and σ_{ext} are the absorption and extinction coefficients, respectively, and g is the asymmetry parameter (the average cosine of the phase function of the medium).

According to Eqs. (18) and (25) in Kokhanovsky and Zege (2004), the extinction coefficients of particles can be expressed as follows:

$$\sigma_{ext} = \frac{l_{tr}}{1-g} = \frac{3C_v}{2r_{eff}}, \quad (12)$$

where l_{tr} is the photon transport path length, C_v is the volumetric snow particle concentration, and r_{eff} is the effective grain size, which equals the radius of the volume-to-surface equivalent sphere: $r_{eff} = \frac{3\bar{V}}{4\bar{A}}$, where $\bar{V}$ and $\bar{A}$ are the average volume and cross-sectional (geometric shadow) area of snow grains, respectively.

The absorption coefficient σ_{abs} in Eq. (11) for arbitrarily shaped and weakly absorbing large grains is proportional to the volume concentration (Kokhanovsky and Zege, 2004):

$$\sigma_{abs} = B \cdot \frac{4\pi k(\lambda)}{\lambda} \cdot C_v, \quad (13)$$

where $k(\lambda)$ is the imaginary component of the complex refractive index for ice, and B is a factor that is only dependent on particle shape. The theory based on the ray-optics approach shows that g in Eq. (11) and B in Eq. (13) are 0.89 and 1.27 for spheres, 0.84 and 1.50 for hexagonal plates or columns, and 0.75 and 1.84 for fractal grains, respectively.

The total absorption coefficient, σ_{abs}, can be derived from the absorption by snow, σ_{abs}^{snow}, and the absorption by ILAPs (σ_{abs}^{BC}, σ_{abs}^{MD}, and σ_{abs}^{OC}):

$$\sigma_{abs} = \sigma_{abs}^{snow} + \sigma_{abs}^{BC} + \sigma_{abs}^{MD} + \sigma_{abs}^{OC}. \quad (14)$$

The hemispherical reflectance with a zenith angle v_0 can be expressed as follows:

$$
\begin{aligned}
R_{\mathrm{d}}(\lambda) &= \exp\Big(-4 \\
&\cdot\sqrt{\frac{4B}{9(1-g)}\cdot\frac{2\pi\cdot r_{\mathrm{eff}}}{\lambda}\cdot k(\lambda)+\frac{\rho_{\mathrm{ice}}\cdot 2r_{\mathrm{eff}}}{9(1-g)}\cdot \mathrm{MAC}^{\mathrm{BC}}_{\mathrm{abs}}\cdot \mathrm{C}^{*}_{\mathrm{BC}}+\frac{\rho_{\mathrm{ice}}\cdot 2r_{\mathrm{eff}}}{9(1-g)}\cdot \mathrm{MAC}^{\mathrm{MD}}_{\mathrm{abs}}\cdot \mathrm{C}^{*}_{\mathrm{MD}}+\frac{\rho_{\mathrm{ice}}\cdot 2r_{\mathrm{eff}}}{9(1-g)}\cdot \mathrm{MAC}^{\mathrm{OC}}_{\mathrm{abs}}\cdot \mathrm{C}^{*}_{\mathrm{OC}}} \\
&\cdot\frac{3}{7}(1+2\cos v_0)\Big) \\
&= \exp\Big(-\sqrt{94.746\cdot\frac{r_{\mathrm{eff}}}{\lambda}\cdot k(\lambda)+5.163\cdot r_{\mathrm{eff}}\cdot(\mathrm{MAC}^{\mathrm{BC}}_{\mathrm{abs}}\cdot \mathrm{C}^{*}_{\mathrm{BC}}+\mathrm{MAC}^{\mathrm{MD}}_{\mathrm{abs}}\cdot \mathrm{C}^{*}_{\mathrm{MD}}+\mathrm{MAC}^{\mathrm{OC}}_{\mathrm{abs}}\cdot \mathrm{C}^{*}_{\mathrm{OC}})}\\
&\cdot(1+2\cos v_0)\Big),\ \text{for spherical grains;} \\
&= \exp\Big(-4.95\cdot\sqrt{\frac{\pi\cdot r_{\mathrm{eff}}\cdot\left(k(\lambda)+\alpha\cdot \mathrm{C}^{*}_{\mathrm{BC}}+\beta\cdot \mathrm{C}^{*}_{\mathrm{MD}}+\chi\cdot \mathrm{C}^{*}_{\mathrm{OC}}\right)}{\lambda}}\\
&\cdot(1+2\cos v_0)\Big),\ \text{for hexagonal grains;} \\
&= \exp\Big(-4.38\cdot\sqrt{\frac{\pi\cdot r_{\mathrm{eff}}\cdot\left(k(\lambda)+\alpha\cdot \mathrm{C}^{*}_{\mathrm{BC}}+\beta\cdot \mathrm{C}^{*}_{\mathrm{MD}}+\chi\cdot \mathrm{C}^{*}_{\mathrm{OC}}\right)}{\lambda}}\\
&\cdot(1+2\cos v_0)\Big),\ \text{for fractal grains.}
\end{aligned}
\tag{15}
$$

Previous studies have also shown that the spectral snow albedo is more sensitive to snow grain size and light conditions than BC contamination and snow depths at near-infrared wavelengths (Warren, 1982). Therefore, the snow grain optical effective radius (R_{eff}) was retrieved based on the spectral albedo measured at $\lambda = 1.3\,\mu\mathrm{m}$, where snow grain size dominates the snow albedo variations and the effects of ILAPs at this wavelength are negligible (Warren and Wiscombe, 1980).

3 Results

3.1 The spatial distribution of AOD

AOD is a major optical parameter for aerosol particles and a key factor affecting global climate (Holben et al., 1991, 2001, 2006; Smith et al., 2014; Srivastava and Bhardwaj, 2014). Most of the snow samples were collected in the afternoon at the Aqua-MODIS (13:30 LT) overpass time in order to compare the local AODs at sampling sites by using a spectroradiometer with the satellite remote sensing. The AOD spatial distribution derived from the Aqua-MODIS satellite over northern China associated with sampling site numbers is shown in Fig. 1 during this snow survey. The average AOD in the studied area ranged from 0.1 to 1.0 and exhibited strong spatial inhomogeneity. The largest AOD values (up to approximately 1.0) retrieved from the MODIS satellite were associated with anthropogenic pollution over northeastern China during the 2014 sampling period. These large values, which exceeded 0.6, were related to local air pollution from industrial areas (Che et al., 2015; P. Wang et al., 2010). In contrast, the MODIS-Aqua results indicate that the smallest AOD values (as low as 0.1) at 550 nm were found over the Gobi desert in Inner Mongolia and were related to strong winter winds. Similar patterns in the retrieved MODIS AOD were found by Zhao et al. (2014) and Zhang et al. (2013b). Although previous studies have indicated that AOD values across northeastern China are among the highest in East Asia (Ax et al., 1970; Bi et al., 2014; Che et al., 2009; Routray et al., 2013; Wang et al., 2013b; Xia et al., 2005, 2007), field experiments of aerosol optical properties across northeastern China were limited. Compared with the retrieved AOD by remote sensing, the surface measurements of AOD were also conducted during this snow survey (Fig. 2). Generally, the measured AOD gradually increased from inner Mongolian regions to the industrial areas across northeastern China. In Inner Mongolia, the average AOD was less than 0.25 for sites 90 to 93 under clear sky conditions. We found a large discrepancy of 40–50 % in the same area within the 1 h measurements collected from sites 95a and 95b, which could be possibly correlated with regional biomass burning. However, AOD exceeded 0.3 at sites 98 and 101, which were significantly influenced by anthropogenic air pollution from industrial areas across northern China. MODIS active fires were often spatially distributed over northeastern China and mainly resulted from human activities during cold seasons.

3.2 Contributions to light absorption by ILAPs

The aged surface snow samples were collected at three sites and fresh surface snow samples were collected at the other sites during this snow survey conducted in January 2014. $\mathrm{C}^{\mathrm{est}}_{\mathrm{BC}}$, $\mathrm{C}^{\mathrm{max}}_{\mathrm{BC}}$, $\mathrm{C}^{\mathrm{equiv}}_{\mathrm{BC}}$, $\mathrm{f}^{\mathrm{est}}_{\text{non-BC}}$, $\mathrm{\AA}_{\mathrm{tot}}$, and snow parameters, such as snow depth, snow density, measured snow grain radius (R_{m}), and snow temperature, are given in Table 1 and Fig. 3 for each snow layer following Wang et al. (2013a). In Inner Mongolia, the snow cover was thin and patchy. The average snow depth at sites 90, 91, 93, and 94 was less than 10 cm, which was significantly smaller than those (13 to 20 cm) at sites 95–97 near the northern border of China. The snow samples were collected from drifted snow in Inner Mongolia, and the mass loadings of ILAPs in seasonal snow are mainly due to blowing soil dust. Therefore, the vertical profiles of snow samples mixed with blowing soil from these sites are insufficient to represent the seasonal evolution of wet and dry deposition to snow (Wang et al., 2013a). However, the light absorption of ILAPs is still dominated by OC in these regions, which has been illustrated in the following section. The maximum snow depth was found to be 46 cm at site 102 inside a forest near the Changbai Shan. Snow depth varied from 13 to 46 cm at sites 98 to 102 with an average of 27 cm. R_{m} of the snow samples varied considerably from 0.07 to 1.3 mm. R_{m} increased with the snow depth from the surface to the bottom, larger than recorded in previous studies because of snow melting by solar radiation and the ILAPs (Hadley and Kirchstetter, 2012; Motoyoshi et al., 2005; Painter et al., 2013; Pedersen et al., 2015). The snow density exhibited little geographical variation across northern China at 0.13 to $0.38\,\mathrm{g\,cm^{-3}}$. High snow densities resulted from melting or snow aging. Similar snow densities have been found in the Xinjiang region in northern China (Ye et al., 2012). At site 90, we only collected one layer of snow samples from central Inner Mongolia, and $\mathrm{C}^{\mathrm{est}}_{\mathrm{BC}}$ was $330\,\mathrm{ng\,g^{-1}}$ for aged snow.

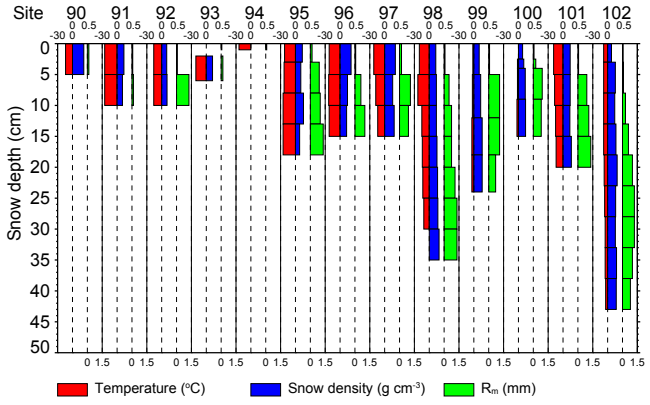

Figure 3. Vertical temperature, snow density, and measured snow grain radius (R_m) profiles at each site during the 2014 Chinese snow survey.

Along the northern Chinese border at sites 91–95, C_{BC}^{est} in the cleanest snow ranged from 30 to 260 ng g^{-1}, with only a few values exceeding 200 ng g^{-1}. The $f_{non\text{-}BC}^{est}$ value varied remarkably from 29 to 78 %, although BC was still a major absorber in this region. Heavily polluted sites were located in industrial regions across northeastern China (sites 99–102). The surface snow C_{BC}^{est} in this region ranged from 510 to 3700 ng g^{-1}, and the highest C_{BC}^{est} in the subsurface layer of the four sites was 2900 ng g^{-1} (Table 1). In addition, $f_{non\text{-}BC}^{est}$ was typically 35–74 %, indicating significant light-absorbing contributions by OC and MD from human activity in the heavily polluted areas. $Å_{tot}$ ranged from 2.1 to 4.8. A higher $Å_{tot}$ is a good indicator of soil dust, which is primarily driven by the composition of mineral or soil dust. In contrast, a lower $Å_{tot}$ of 0.8–1.2 indicates that ILAPs in the snow are dominated by BC (Bergstrom et al., 2002; Bond et al., 1999).

To better understand the distribution of C_{BC}^{est} in seasonal snow across northern China, the spatial distribution of C_{BC}^{est} in the surface and average snow measured during this snow survey is shown in Fig. 4. The spatial distributions of C_{BC}^{est} in the surface and average snow measured using the ISSW spectrophotometer during the 2014 survey generally ranged from 50 to 3700 and 60 to 1600 ng g^{-1}, with medium values of 260 and 260 ng g^{-1}, respectively. These variations in C_{BC}^{est} were very similar to those of the previous snow campaign by Wang et al. (2013a); however, they were much higher than those in the Xinjiang region of northwestern China (Ye et al., 2012), along the southern edge of the Tibetan Plateau (Cong et al., 2015), and across North America (Doherty et al., 2014).

Figure 5 compares C_{BC}^{est} values measured via the ISSW method with the calculations during 2010 (Wang et al., 2013a) and 2014 snow surveys. The two results agreed very well ($R^2 = 0.99$), indicating that Eq. (7) worked well for this measurement, and the C_{BC}^{est} measured via the ISSW method was reliable. To compare with the mixing ratio of OC calculated from Eq. (7), we used the calculated C_{BC}^{est} listed in Figs. 6–7 and Table 2 in the following sections.

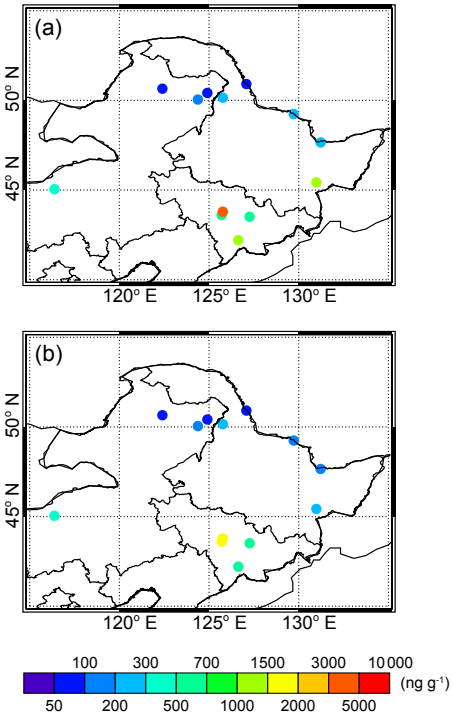

Figure 4. The spatial distribution of C_{BC}^{est} in the **(a)** surface and **(b)** average snow in 2014 across northeastern China.

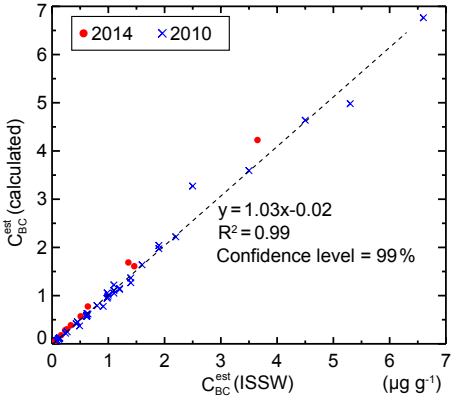

Figure 5. Comparisons between the calculated and optically measured C_{BC}^{est} in surface snow during the 2010 and 2014 snow surveys. The datasets of measured C_{BC}^{est} in 2010 from sites 3–40 were reprinted from Wang et al. (2013a).

In Fig. 6, the sampling areas were located in grasslands, croplands, and urban and built-up regions across northern China that were likely influenced by human activity (Huang et al., 2015). According to Table 2 and Fig. 6, the NH_4^+ concentrations emitted from agricultural sources at all sites accounted for less than 2.8 % because the sites were positioned 50 km from cities. However, large fractions of both SO_4^{2-}

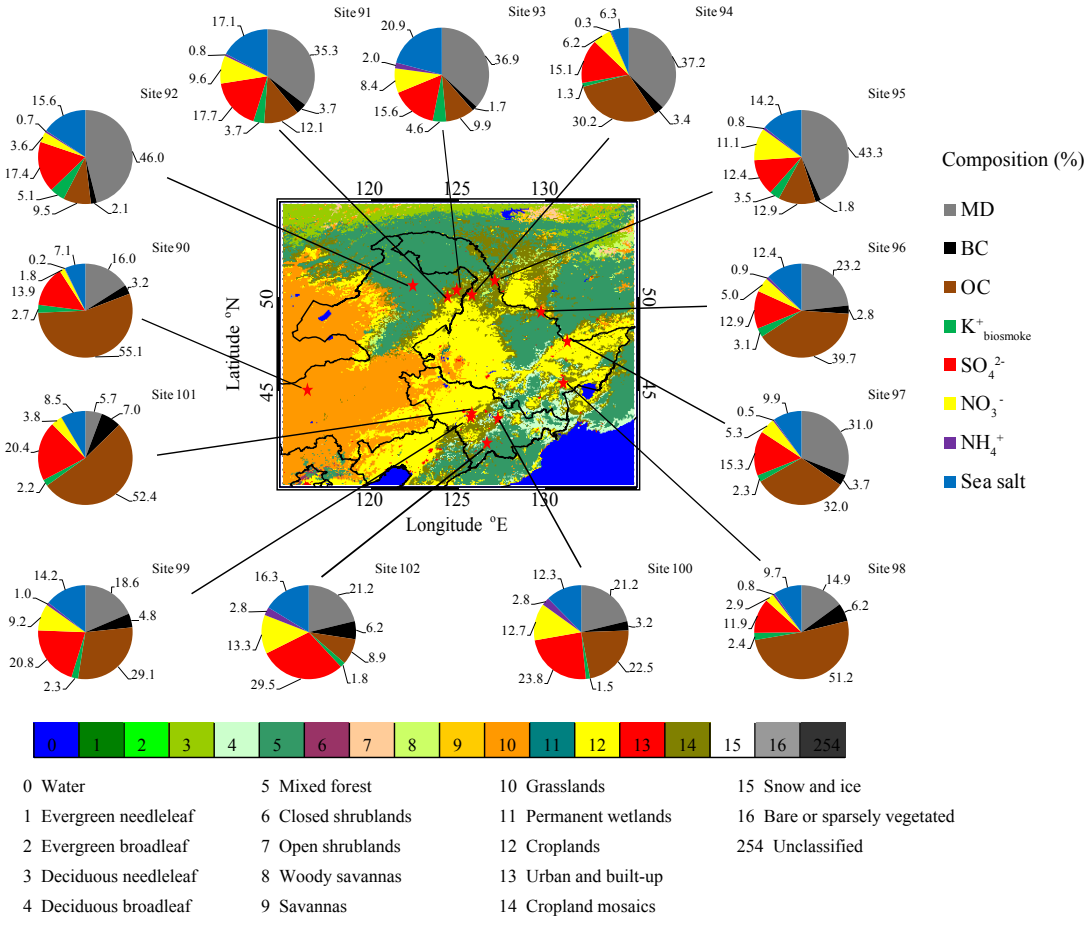

Figure 6. The major components include MD, BC, OC, $K^+_{Biosmoke}$, secondary ions (SO_4^{2-}, NO_3^-, and NH_4^+), and sea salt in the surface snow samples collected in January 2014. The distribution of 17 different surface vegetation types retrieved from MODIS global land cover type product (MCD12C1) with 0.05 spatial resolution was used in this study. The datasets of SO_4^{2-}, NO_3^-, and NH_4^+ were reprinted from Wang et al. (2015).

Table 2. Chemical species (ng g^{-1}) in surface snow for sites across northeastern China in January 2014. The datasets of SO_4^{2-}, NO_3^-, and NH_4^+ were reprinted from Wang et al. (2015).

Site	MD	BC	OC	$K^+_{biosmoke}$	SO_4^{2-}	NO_3^-	NH_4^+	Sea salt
90	1900	380	6700	327	1685	213	22	868
91	1700	180	590	179	853	465	36	827
92	1300	60	280	150	511	105	19	456
93	1700	80	450	213	718	387	90	960
94	3300	300	2700	118	1335	550	28	554
95	2000	90	600	164	587	523	39	669
96	2300	280	3900	309	1285	493	91	1227
97	2400	280	2400	173	1163	407	38	753
98	3900	1600	13 300	633	3096	747	195	2516
99	3000	770	4700	372	3379	1492	155	2310
100	3800	570	4000	260	4237	2258	487	2195
101	3500	4200	32 000	1337	12 382	2364	–	5131
102	5800	1700	2400	488	8034	3631	769	4420

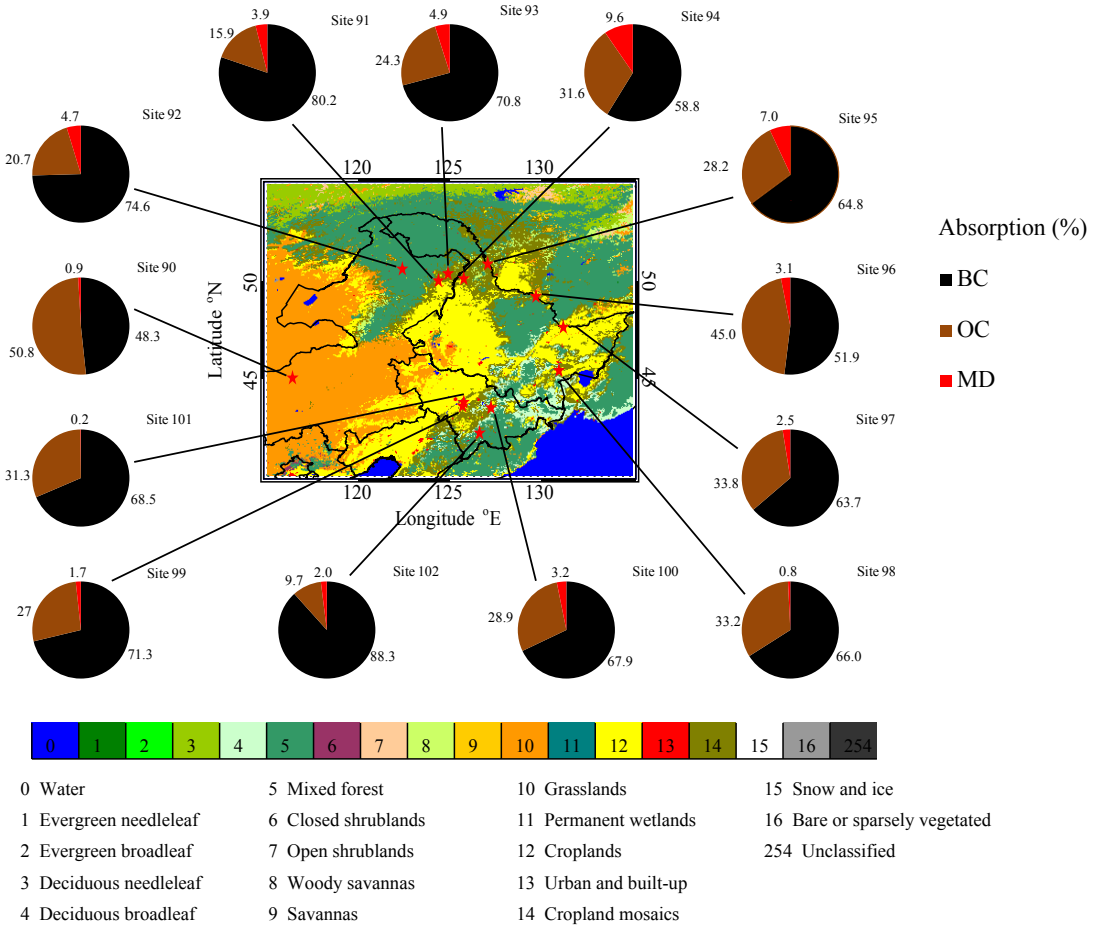

Figure 7. The light absorption of ILAPs in surface snow in January 2014. The distribution of 17 different surface vegetation types retrieved from MODIS global land cover type product (MCD12C1) with 0.05 spatial resolution were used in this study.

and NO_3^- were observed, varying from 14.8 to 42.8 % at all sites, with the highest fraction of 24.2–42.8 % found in industrial areas. These results show that SO_4^{2-} and NO_3^- made the greatest contributions to the total chemical concentration in the surface snow as a result of significant anthropogenic emissions of fossil-fuel combustion in heavy industrial areas. More specifically, the largest MD contribution ranged from 35.3 to 46 % at sites 91 to 95 due to strong winds during winter, while the MD fractions were only 5.7 to 31 % at the other sites. Fractions of BC and OC were similar to those above, showing that biomass burning was a major source during winter in the sampling region. Zhang et al. (2013b) showed that OC and BC fractions vary more widely in the winter than other seasons due to industrial activity in China. Sulfate peaks were found in summer (15.4 %), whereas nitrate peaks were observed in spring (11.1 %). $K^+_{Biosmoke}$ was found to be a good tracer of biomass burning, ranging from 1.3 to 5.1 % along the northern Chinese border compared to lower values found at lower latitudes (1.5–2.3 %), and it exhibited much higher contributions in Inner Mongolia and along the northern Chinese border due to increased emissions from cooking, open fires, and agricultural activities. The fraction of sea salt was found to range from 6.3 to 20.9 %. Wang et al. (2015) showed that higher Cl^- / Na^+ ratios in seasonal snow found in the 2014 Chinese survey were 1–2 times greater than those of seawater, implying that they constituted a significant source of anthropogenic Cl^-.

Light absorption by ILAPs can be determined from ISSW measurements combined with chemical analysis of Fe concentration, assuming that the light absorption of dust is dominated by Fe (Wang et al., 2013a). However, Fe can also originate from industrial emissions, such as the metal and steel industries (Hegg et al., 2010; Ofosu et al., 2012). Doherty et al. (2014) used a similar method to distinguish contributions of ILAPs in snow in central North America. Although heavy MD loading was observed in the 2014 snow survey, the fraction of light absorption due to MD (assumed to exist as goethite) was generally less than 10 % across northeastern China (Fig. 7), which was much smaller than that observed in the Qilian Shan (e.g., Fig. 11 of Wang et al., 2013a). Here,

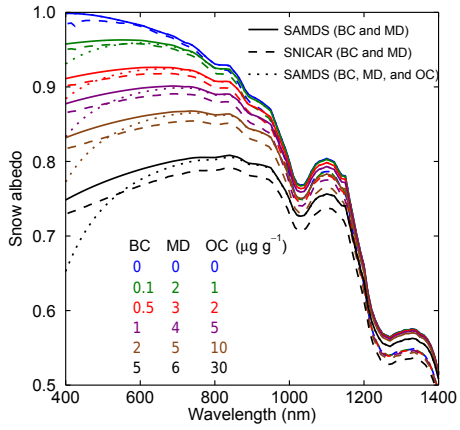

Figure 8. Spectral albedo of snow with different contaminants for a 60° solar zenith angle and a 100 µm R_{eff}. Solid and dashed lines show the SAMDS and SNICAR model predictions for BC and MD. Dotted lines show the SAMDS model predictions for all ILAPs, including BC, MD, and OC.

light absorption was mainly dominated by BC and OC in snow in January 2014. By contrast, the fraction of light absorption due to BC varied from 48.3 to 88.3 % at all sites, with only one site dominated by OC (site 90 in central Inner Mongolia). Compared to the light absorption patterns in the Qilian Shan, MD played a less significant role in particulate light absorption in snow across the northeastern Chinese sampling areas.

3.3 Simulations of snow albedo

Snow albedo reduction due to BC has been examined in previous studies (Brandt et al., 2011; Hadley and Kirchstetter, 2012; Yasunari et al., 2010). Here, a new radiative transfer model (SAMDS) based on the asymptotic radiative transfer theory is developed to assess the effects of various factors on snow albedo, including ILAPs in snow, the snow grain shapes, and the internal–external mixing of BC and snow. The snow albedos derived from the SNICAR and SAMDS models are presented in Fig. 8. We ran the models at a solar zenith angle θ of 60°, which is comparable with our experimental method for measuring snow albedo across northeastern China. The BC MAC used in the two models was 7.5 $m^2\,g^{-1}$ at 550 nm, which was assumed in the most recent climate assessment and is appropriate for freshly emitted BC (Bond and Bergstrom, 2006; Bond et al., 2013; Warren, 1982). Mixing ratios of BC, MD, and OC were chosen to vary in the following ranges: 0.1–5, 2–6, and 1–30 µg g^{-1}, respectively, encompassing the values measured in snow surfaces across northeastern China in this and previous studies (Doherty et al., 2010, 2014; Wang et al., 2013a, 2014; Warren and Wiscombe, 1980; Ye et al., 2012). Results showed that the albedo of fresh snow at 550 nm with R_{eff} of 100 µm simulated by SAMDS is generally in the range of 0.95–0.75 for ILAP-contaminated snow across northeastern China (Fig. 8). The spectral albedos of pure snow derived from the SNICAR (dashed lines) and SAMDS (solid lines) models agree well. However, there is a slight tendency for the SNICAR model values to become lower than SAMDS model values when BC and MD are considered. The 1–3 % deviation between the SNICAR- and SAMDS-modeled snow albedos at 550 nm for BC mixing ratios of 1–5 µg g^{-1} indicates that albedo reduction by ILAPs in the SNICAR model was greater than in the SAMDS model. This deviation is in part due to the different parameterization of snow grain shapes, mixing states of snow and BC, and physical-chemical properties of impurities between the two models (Zhang et al., 2017). More notably, snow albedos decreased significantly within the UV-visible wavelength, especially for the higher OC (dotted lines) mixing ratios in Fig. 8. This may be attributed to the fact that OC strongly absorbs UV-visible radiation and masks BC absorption for high AAE of OC, which decreases remarkably with increasing wavelengths (Warren and Wiscombe, 1980).

As shown in Fig. 9, we also estimated the reduction in the spectrally weighted snow albedo for different R_{eff} values using the SNICAR and SAMDS models. A larger reduction in snow albedo by both BC- and MD-contaminated snow was found for larger snow grains (Fig. 9a–b). For example, snow albedo reduction attributable to 1, 1, and 10 µg g^{-1} for BC, MD, and OC, respectively, was 37, 41, and 38 % greater in 200 µm snow grains (0.081, 0.0019, and 0.047) than in 100 µm snow grains (0.059, 0.0013, and 0.034). Both the SNICAR and SAMDS models indicated that the snow albedo is more sensitive to BC, especially at low ILAP mixing ratios. For example, 200 ng g^{-1} of BC decreased 0.03 snow albedo at R_{eff} of 200 µm, which is much larger than the snow albedo reduction of 0.003 and 0.018 by 2000 ng g^{-1} of MD and OC at R_{eff} of 200 µm. As Hadley and Kirchstetter (2012) noted, compared with pure 55 µm snow grains, 300 ng g^{-1} of BC contamination and growth of R_{eff} to 110 µm caused a net albedo reduction of 0.11 (from 0.82 to 0.71) or 61 % more solar energy absorption by snow. The difference in snow albedo reduction between SNICAR and SAMDS models increased with increasing BC mixing ratio or R_{eff} (Fig. 9a). However, the snow albedo reduction simulated by SNICAR is not always larger than that by SAMDS when the input contaminant is MD instead of BC (Fig. 9b). For example, for R_{eff} of 100 µm, the snow albedo reduction from SAMDS is higher than that from SNICAR at MD mixing ratio < 2600 ng g^{-1} but lower at MD mixing ratio > 2600 ng g^{-1}. The turning point of MD mixing ratio is not constant and depends on the value of R_{eff}. This phenomenon may be a result of the different input optical properties of MD between SAMDS and SNICAR models (Flanner et al., 2007; Zhang et al., 2017). The SAMDS model also considers the effect of OC on snow albedo, while SNICAR model does not. The albedo reduction by OC is non-negligible due to its high loading. As shown, 5000 ng g^{-1} of OC was found to reduce the snow albedo by 0.016–0.059 depending on the snow grain size (50–800 µm).

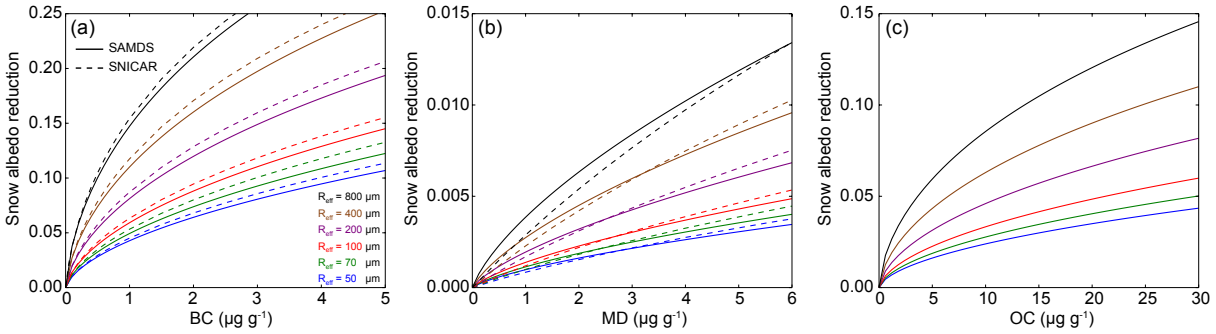

Figure 9. Spectrally weighted snow albedo reduction over the 400–1400 nm solar spectrum attributed to **(a)** BC, **(b)** MD, and **(c)** OC computed as the albedo of pure snow minus the albedo of contaminated snow for a 60° solar zenith angle. Solid and dashed lines show the SAMDS and SNICAR model predictions. The MAC values of BC, OC, and Fe were assumed to be 7.5, 0.3, and 0.9 $m^2\ g^{-1}$ at 550 nm, respectively, in the SAMDS model.

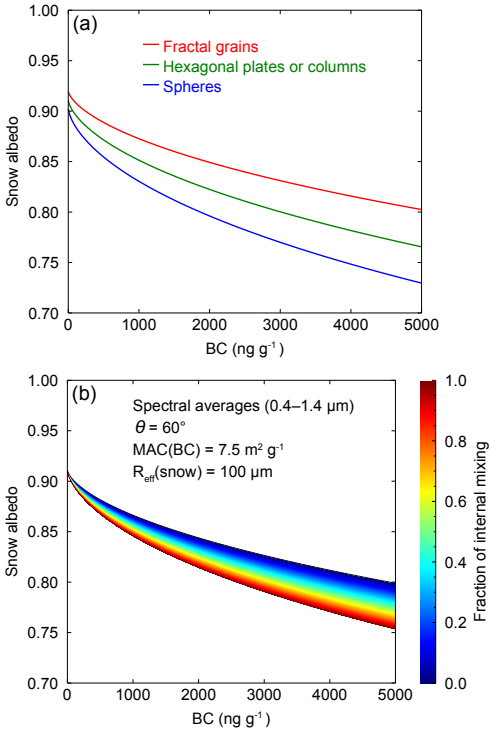

Figure 10. Spectral albedo of snow as a function of BC mixing ratios in snow by using SMDAS model for **(a)** the irregular morphology of snow grains (fractal grains, hexagonal plates or columns, and spheres), **(b)** internal–external mixing of BC and hexagonal plate or column snow grains. Also shown are model parameters, including integrate spectral wavelengths (400–1400 nm), solar zenith angle (θ), mass absorption coefficient (MAC) of BC, and snow grain optical effective radius (R_{eff}).

Previous studies have also indicated that the mixing ratio of BC (10–100 ng g^{-1}) in snow may decrease its albedo by 1–5 % (Hadley and Kirchstetter, 2012; Warren and Wiscombe, 1980). Liou et al. (2011) demonstrated that a small BC particle on the order of 1 μm internally mixed with snow grains could effectively reduce visible snow albedo by as much as 5–10 %. They also found that internal mixing of BC in snow reduces snow albedo more substantially than external mixing, and the snow grain shape plays a critical role in snow albedo calculations through its forward scattering strength by modeling the positions of BC internally mixed with different snow grain types (Liou et al., 2014). Figure 10a illustrates the effect of snow shape (fractal grain, hexagonal plate or column, and sphere) on snow albedo at the spectral wavelengths of 400–1400 nm with R_{eff} of 100 μm simulated by the SAMDS model. As shown, the differences in snow albedo caused by three snow shapes are remarkable. The snow albedo for spherical snow grains is higher than that for the other two shapes, which is because the scattering by spherical snow grains is more in the forward direction and less to the sides, resulting in a larger g and a smaller B, as discussed in Sect. 2.5. In addition, the snow albedo reduction for aged snow such as spherical snow grains is gradually larger than fresh snow such as fractal snow grains and hexagonal plate or column snow grains with the increased BC in snow. It shows that snow albedo by spherical snow grains is typically lower by 0.017–0.073 than the fractal snow grains, and by 0.008–0.036 than the hexagonal plate or column snow grains as a function of BC mixing ratios (0–5000 ng g^{-1}). Dang et al. (2016) assessed the effects of snow grain shapes on snow albedo using the asymmetry factors g of nonspherical ice crystal developed by Fu (2007). They obtained similar results showing that the albedo reduction caused by 100 ng g^{-1} of BC for spherical snow grains is larger by 0.007 than nonspherical snow grains with the same area-to-mass ratio for R_{eff} of 100 μm. Figure 10b shows the spectral albedo of snow for the internal–external mixing of BC and snow with R_{eff} of 100 μm for a solar zenith angle θ of 60° as a function of BC mixing ratio. For a given shape (hexagonal plates or columns), we found that snow albedo as a function of BC mixing ratios calculated from this study decreases as the fraction of the internal mixing increases (Fig. 10b). In previous studies, the BC mixing ratios in seasonal snow were up to

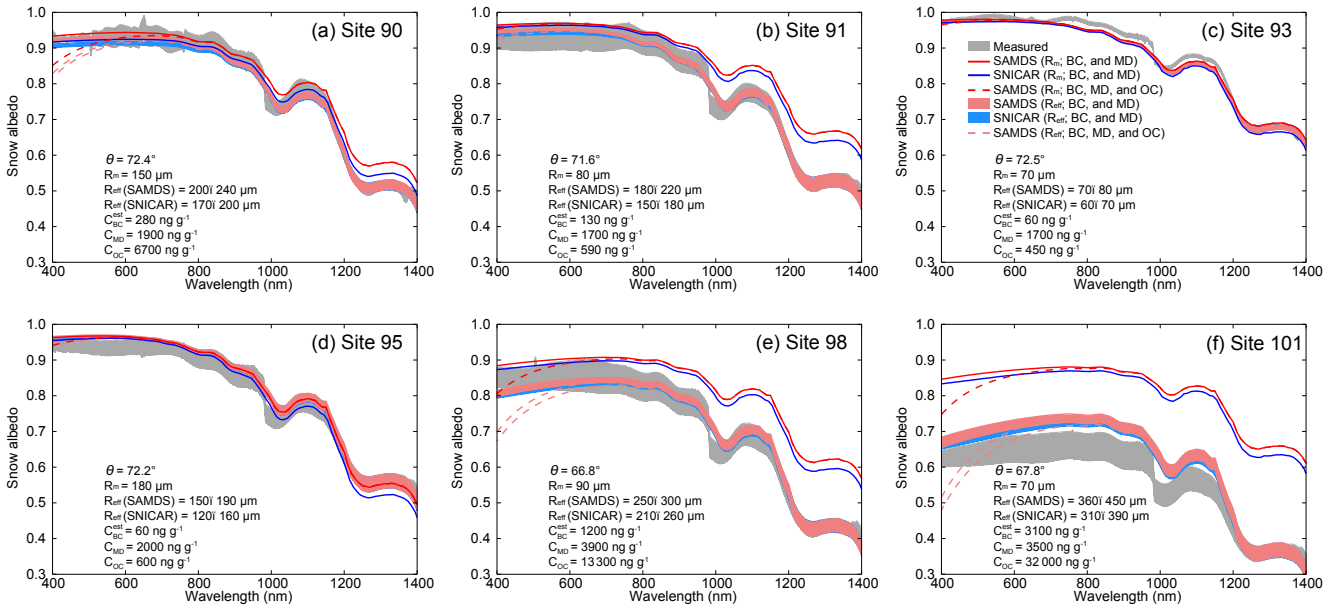

Figure 11. Measured and modeled spectral albedos of snow at sites **(a)** 90, **(b)** 91, **(c)** 93, **(d)** 95, **(e)** 98, and **(f)** 101. Shaded gray bands correspond to measured spectral albedos using spectroradiometer. Solid red and blue lines correspond to spectral albedos simulated by the SAMDS and SNICAR models with measured snow grain radii (R_m), and shaded light red and blue bands correspond to the albedos with calculated snow grain optical effective radii (R_{eff}). Contaminants only include BC and MD in the SAMDS and SNICAR models. In the SNICAR model, the ratio of Fe in dust was assumed to be 2.8 %. Dashed red lines are similar to solid red lines, although OC should be added to the list of contaminants in the SAMDS model.

3000 ng g^{-1} due to heavy industrial activities across northern China, but the lowest mixing ratios of BC were found in the remote northeastern area on the border of Siberia, with a median value in surface snow of 100 ng g^{-1} (Huang et al., 2011; Wang et al., 2013a, 2014; Ye et al., 2012). As a result, snow albedo by internal mixing of BC and snow is lower than external mixing by up to 0.036 for 3000 ng g^{-1} BC in snow in the heavy industrial regions across northeastern China, whereas it is 0.005 for 100 ng g^{-1} BC in snow in northern China near the border of Siberia. We indicated that the snow grain shape effect on snow albedo between spherical snow grains and fractal snow grains is relatively larger than the effect of the internal–external mixing of BC and snow as a function of the BC mixing ratios. However, He et al. (2014) also pointed out that the snow albedo reductions computed by previous models under assorted assumptions vary by a factor of 2 to 5.

3.4 Comparison between the observed and modeled snow albedo

Although the snow albedo reduction due to ILAPs has been investigated by model simulations in recent studies (Brandt et al., 2011; Flanner et al., 2007; Hadley and Kirchstetter, 2012; Liou et al., 2011, 2014; Warren and Wiscombe, 1980), we noted that there were still limited field campaigns on collecting snow samples and measuring ILAPs in seasonal snow associated with the snow albedo reduction at middle latitudes in the Northern Hemisphere (Doherty et al., 2010, 2014; Wang et al., 2013a; Ye et al., 2012). Snow albedo under clear sky conditions was measured at six sites, which was compared to SNICAR and SAMDS model simulations based on two-stream radiative transfer solution of Toon et al. (1989) (Fig. 11). Model input parameters, including θ, R_m, R_{eff}, and the mixing ratios of BC (C^{est}_{BC}), MD (C_{MD}), and OC (C_{OC}), are also displayed in Fig. 11. The MAC of BC used in the ISSW is 6.3 m^2 g^{-1} at 550 nm, although a value of 7.5 is used in the SNICAR and SAMDS models. Thus, the value of C^{est}_{BC} was corrected by dividing it by 1.19 (see Fig. 11) when BC was used as the input parameter to the snow albedo models (Wang et al., 2013a). The snow albedos measured at 550 nm varied considerably from 0.99 to 0.61 due to different mixing ratios of ILAPs and snow parameters such as snow grain size. The snow albedos predicted by the SNICAR and SAMDS models agreed well at most sites based on the same input parameters. The snow albedos of the SNICAR and SAMDS models retrieved with R_m complemented the surface measurements for lower values of C^{est}_{BC}, C_{MD}, and C_{OC} (Fig. 11a–d). The highest C^{est}_{BC} values were 1500 ng g^{-1} (corrected value of 1200 ng g^{-1}) and 3700 ng g^{-1} (corrected value of 3100 ng g^{-1}) at sites 98 and 101, respectively, across industrial regions. The OC and MD mixing ratios were as high as 32 000 and 3900 ng g^{-1}, respectively, in this region. Therefore, we found a larger difference in snow albedo of up to 0.2 at higher C^{est}_{BC}, C_{MD}, and

C_{OC} values between the surface measurements and the modeled albedos by both SAMDS and SNICAR models with the input of R_m (solid red and blue lines in Fig. 11e–f). When the snow albedo at the inferred wavelength simulated by using R_m was not accounted for, we also calculated the snow albedos using the SAMDS and SNICAR models with R_{eff} as shown in Fig. 11 (shaded light red and blue bands). Results showed that compared with the snow albedos simulated using R_m, these values were more approximate to the surface measurements, especially at near-infrared wavelengths, although still slightly higher than the surface measurements (shaded gray bands). This may be attributed to the fact that R_{eff} at these two sampling sites was much larger than R_m. We assumed that, for the same snow grains, ILAPs are able to enhance the R_{eff} in spite of the same R_m, which should be verified by future field measurements of snow albedos.

Results shown in Figs. 9 and 11 confirm that BC, OC, and MD are three main types of ILAPs in snow that can reduce spectral snow albedo. The magnitudes of snow albedo reduction due to ILAPs found in our measurements were generally comparable to those produced by the SAMDS and SNICAR models (Flanner et al., 2007; Zhang et al., 2017). When the mixing ratios of ILAPs are not quite high, we indicate that 100–500 ng g^{-1} of BC can lower the snow albedo by 0.014–0.039 relative to pure snow with a snow grain size of 100 µm, according to our snow field campaign. Furthermore, MD was found to be a weak absorber due to its lower MD MAC, supporting previous observations made by Warren and Wiscombe (1980). The OC MAC is also lower and comparable to that of the MD. A clear decreasing trend in the surface snow albedo due to the high ambient mixing ratios of OC from Inner Mongolia to northeastern China was found. The radiative transfer model results presented by Zhang et al. (2017) and measurement results of this study show that the spectral albedo of snow reduction due to the increased OC mixing ratios (above 20 µg g^{-1}) is larger by a factor of 3 if assuming the snow grain size of 800 compared to 100 µm.

4 Conclusions

High AODs measured using a sunphotometer and remote sensing devices showed continued heavy pollution in industrial regions across northern China. The measured C_{BC}^{est} through the 2014 survey via the ISSW spectrophotometer in surface and average snow were much larger than those of previous snow field campaigns. Light absorption was likely dominated by BC and OC in seasonal snow during the entire campaign, as demonstrated with reasonably assumed values of MACs for BC, OC, and Fe.

Model simulation results indicated that the snow albedo for spherical snow grains is typically lower than that for the fractal snow grains and hexagonal plate or column snow grains with R_{eff} of 100 µm. The internal mixing of BC and snow absorbs substantially more light than external mixing. Snow albedos simulated using the SNICAR and SAMDS models using R_m agreed well with the measured ones from the spectroradiometer at low mixing ratios of BC, MD, and OC, but with large discrepancies for heavy loading of ILAPs in snow. Snow albedo reduction simulated by SMDAS and SNICAR models is significantly higher using R_{eff} of snow grains than using R_m, especially in the case of near-infrared wavelengths. The mixing ratio of OC should be added as an input parameter to the SNICAR model for determining snow albedo.

Future snow survey studies across northern China should be performed to address the large variations in ILAPs in seasonal snow across the region. Additional model simulations and comparisons with measurements are needed to verify R_{eff} effect under the scenario of high mixing ratios of ILAPs in snow.

5 Data availability

All data sets and codes used to produce this study can be obtained by contacting Xin Wang (wxin@lzu.edu.cn). The MODIS data used in this study are available at Aerosol Product, https://modis.gsfc.nasa.gov/data/dataprod/mod04.php; Active Fire Product, http://earthdata.nasa.gov/firms; and Land Cover Type Product, https://lpdaac.usgs.gov/dataset_discovery/modis/modis_products_table/mcd12c1.

Competing interests. The authors declare that they have no conflict of interest.

Acknowledgements. This research was supported by the Foundation for Innovative Research Groups of the National Natural Science Foundation of China (41521004), the National Natural Science Foundation of China under grant 41522505, and the Fundamental Research Funds for the Central Universities (lzujbky-2015-k01, lzujbky-2016-k06 and lzujbky-2015-3). The MODIS data were obtained from the NASA Earth Observing System Data and Information System, Land Processes Distributed Active Archive Center (LP DAAC) at the USGS Earth Resources Observation and Science (EROS) Center.

Edited by: L. Zhang
Reviewed by: two anonymous referees

References

Alfaro, S. C., Lafon, S., Rajot, J. L., Formenti, P., Gaudichet, A., and Maille, M.: Iron oxides and light absorption by pure desert dust: An experimental study, J. Geophys. Res.-Atmos., 109, D08208, doi:10.1029/2003JD004374, 2004.

Arhami, M., Kuhn, T., Fine, P. M., Delfino, R. J., and Sioutas, C.: Effects of sampling artifacts and operating parameters on

the performance of a semicontinuous particulate elemental carbon/organic carbon monitor, Environ. Sci. Technol., 40, 945–954, 2006.

Ax, W., Malchow, H., Koren, H., and Fischer, H.: Studies on immunological reactions in vitro, Sbornik vedeckych praci Lekarske fakulty Karlovy university v Hradci Kralove, 13, 287–292, 1970.

Bergstrom, R. W., Russell, P. B., and Hignett, P.: Wavelength dependence of the absorption of black carbon particles: Predictions and results from the TARFOX experiment and implications for the aerosol single scattering albedo, J. Atmos. Sci., 59, 567–577, 2002.

Bi, J. R., Huang, J. P., Hu, Z. Y., Holben, B. N., and Guo, Z. Q.: Investigating the aerosol optical and radiative characteristics of heavy haze episodes in Beijing during January of 2013, J. Geophys. Res.-Atmos., 119, 9884–9900, 2014.

Bond, T. C. and Bergstrom, R. W.: Light absorption by carbonaceous particles: An investigative review, Aerosol Sci. Tech., 40, 27–67, 2006.

Bond, T. C., Bussemer, M., Wehner, B., Keller, S., Charlson, R. J., and Heintzenberg, J.: Light absorption by primary particle emissions from a lignite burning plant, Environ. Sci. Technol., 33, 3887–3891, 1999.

Bond, T. C., Doherty, S. J., Fahey, D. W., Forster, P. M., Berntsen, T., DeAngelo, B. J., Flanner, M. G., Ghan, S., Karcher, B., Koch, D., Kinne, S., Kondo, Y., Quinn, P. K., Sarofim, M. C., Schultz, M. G., Schulz, M., Venkataraman, C., Zhang, H., Zhang, S., Bellouin, N., Guttikunda, S. K., Hopke, P. K., Jacobson, M. Z., Kaiser, J. W., Klimont, Z., Lohmann, U., Schwarz, J. P., Shindell, D., Storelvmo, T., Warren, S. G., and Zender, C. S.: Bounding the role of black carbon in the climate system: A scientific assessment, J. Geophys. Res.-Atmos., 118, 5380–5552, 2013.

Brandt, R. E., Warren, S. G., and Clarke, A. D.: A controlled snowmaking experiment testing the relation between black carbon content and reduction of snow albedo, J. Geophys. Res.-Atmos., 116, D08109, doi:10.1029/2010JD015330, 2011.

Cappa, C. D., Onasch, T. B., Massoli, P., Worsnop, D. R., Bates, T. S., Cross, E. S., Davidovits, P., Hakala, J., Hayden, K. L., Jobson, B. T., Kolesar, K. R., Lack, D. A., Lerner, B. M., Li, S. M., Mellon, D., Nuaaman, I., Olfert, J. S., Petaja, T., Quinn, P. K., Song, C., Subramanian, R., Williams, E. J., and Zaveri, R. A.: Radiative Absorption Enhancements Due to the Mixing State of Atmospheric Black Carbon, Science, 337, 1078–1081, 2012.

Carmagnola, C. M., Domine, F., Dumont, M., Wright, P., Strellis, B., Bergin, M., Dibb, J., Picard, G., Libois, Q., Arnaud, L., and Morin, S.: Snow spectral albedo at Summit, Greenland: measurements and numerical simulations based on physical and chemical properties of the snowpack, The Cryosphere, 7, 1139–1160, doi:10.5194/tc-7-1139-2013, 2013.

Che, H. Z., Yang, Z. F., Zhang, X. Y., Zhu, C. Z., Ma, Q. L., Zhou, H. G., and Wang, P.: Study on the aerosol optical properties and their relationship with aerosol chemical compositions over three regional background stations in China, Atmos. Environ., 43, 1093–1099, 2009.

Che, H. Z., Wang, Y. Q., and Sun, J. Y.: Aerosol optical properties at Mt. Waliguan Observatory, China, Atmos. Environ., 45, 6004–6009, 2011.

Che, H. Z., Wang, Y. Q., Sun, J. Y., Zhang, X. C., Zhang, X. Y., and Guo, J. P.: Variation of Aerosol Optical Properties over the Taklimakan Desert in China, Aerosol Air Qual. Res., 13, 777–785, 2013.

Che, H. Z., Zhao, H. J., Wu, Y. F., Xia, X. G., Zhu, J., Wang, H., Wang, Y. Q., Sun, J. Y., Yu, J., Zhang, X. Y., and Shi, G. Y.: Analyses of aerosol optical properties and direct radiative forcing over urban and industrial regions in Northeast China, Meteorol. Atmos. Phys., 127, 345–354, 2015.

Chen, S. Y., Huang, J. P., Zhao, C., Qian, Y., Leung, L. R., and Yang, B.: Modeling the transport and radiative forcing of Taklimakan dust over the Tibetan Plateau: A case study in the summer of 2006, J. Geophys. Res.-Atmos., 118, 797–812, 2013.

Chu, D. A., Kaufman, Y. J., Ichoku, C., Remer, L. A., Tanre, D., and Holben, B. N.: Validation of MODIS aerosol optical depth retrieval over land, Geophys. Res. Lett., 29, 1617, doi:10.1029/2001GL013205, 2002.

Cong, Z., Kang, S., Kawamura, K., Liu, B., Wan, X., Wang, Z., Gao, S., and Fu, P.: Carbonaceous aerosols on the south edge of the Tibetan Plateau: concentrations, seasonality and sources, Atmos. Chem. Phys., 15, 1573–1584, doi:10.5194/acp-15-1573-2015, 2015.

Dang, C. and Hegg, D. A.: Quantifying light absorption by organic carbon in Western North American snow by serial chemical extractions, J. Geophys. Res.-Atmos., 119, 10247–10261, 2014.

Dang, C., Brandt, R. E., and Warren, S. G.: Parameterizations for narrowband and broadband albedo of pure snow and snow containing mineral dust and black carbon, J. Geophys. Res.-Atmos., 120, 5446–5468, 2015.

Dang, C., Fu, Q., and Warren, S. G.: Effect of Snow Grain Shape on Snow Albedo, J. Atmos. Sci., 73, 3573–3583, 2016.

Doherty, S. J., Warren, S. G., Grenfell, T. C., Clarke, A. D., and Brandt, R. E.: Light-absorbing impurities in Arctic snow, Atmos. Chem. Phys., 10, 11647–11680, doi:10.5194/acp-10-11647-2010, 2010.

Doherty, S. J., Dang, C., Hegg, D. A., Zhang, R. D., and Warren, S. G.: Black carbon and other light-absorbing particles in snow of central North America, J. Geophys. Res.-Atmos., 119, 12807–12831, 2014.

Fierce, L., Bond, T. C., Bauer, S. E., Mena, F., and Riemer, N.: Black carbon absorption at the global scale is affected by particle-scale diversity in composition, Nat. Commun., 7, 12361, doi:10.1038/ncomms12361, 2016.

Flanner, M. G., Zender, C. S., Randerson, J. T., and Rasch, P. J.: Present-day climate forcing and response from black carbon in snow, J. Geophys. Res.-Atmos., 112, D11202, doi:10.1029/2006JD008003, 2007.

Flanner, M. G., Zender, C. S., Hess, P. G., Mahowald, N. M., Painter, T. H., Ramanathan, V., and Rasch, P. J.: Springtime warming and reduced snow cover from carbonaceous particles, Atmos. Chem. Phys., 9, 2481–2497, doi:10.5194/acp-9-2481-2009, 2009.

Flanner, M. G., Liu, X., Zhou, C., Penner, J. E., and Jiao, C.: Enhanced solar energy absorption by internally-mixed black carbon in snow grains, Atmos. Chem. Phys., 12, 4699–4721, doi:10.5194/acp-12-4699-2012, 2012.

Friedl, M. A., Sulla-Menashe, D., Tan, B., Schneider, A., Ramankutty, N., Sibley, A., and Huang, X. M.: MODIS Collection 5 global land cover: Algorithm refinements and characterization of new datasets, Remote Sens. Environ., 114, 168–182, 2010.

Fu, Q.: A New Parameterization of an Asymmetry Factor of Cirrus Clouds for Climate Models, J. Atmos. Sci., 64, 4140–4150, 2007.

Grenfell, T. C., Warren, S. G., and Mullen, P. C.: Reflection of Solar-Radiation by the Antarctic Snow Surface at Ultraviolet, Visible, and near-Infrared Wavelengths, J. Geophys. Res.-Atmos., 99, 18669–18684, 1994.

Grenfell, T. C., Doherty, S. J., Clarke, A. D., and Warren, S. G.: Light absorption from particulate impurities in snow and ice determined by spectrophotometric analysis of filters, Appl. Optics, 50, 2037–2048, 2011.

Guan, X., Huang, J., Guo, R., Yu, H., Lin, P., and Zhang, Y.: Role of radiatively forced temperature changes in enhanced semi-arid warming in the cold season over east Asia, Atmos. Chem. Phys., 15, 13777–13786, doi:10.5194/acp-15-13777-2015, 2015.

Hadley, O. L. and Kirchstetter, T. W.: Black-carbon reduction of snow albedo, Nat. Clim. Change, 2, 437–440, 2012.

Hansen, J. and Nazarenko, L.: Soot climate forcing via snow and ice albedos, P. Natl. Acad. Sci. USA, 101, 423–428, 2004.

Hansen, J., Sato, M., Ruedy, R., Nazarenko, L., Lacis, A., Schmidt, G. A., Russell, G., Aleinov, I., Bauer, M., Bauer, S., Bell, N., Cairns, B., Canuto, V., Chandler, M., Cheng, Y., Del Genio, A., Faluvegi, G., Fleming, E., Friend, A., Hall, T., Jackman, C., Kelley, M., Kiang, N., Koch, D., Lean, J., Lerner, J., Lo, K., Menon, S., Miller, R., Minnis, P., Novakov, T., Oinas, V., Perlwitz, J., Perlwitz, J., Rind, D., Romanou, A., Shindell, D., Stone, P., Sun, S., Tausnev, N., Thresher, D., Wielicki, B., Wong, T., Yao, M., and Zhang, S.: Efficacy of climate forcings, J. Geophys. Res.-Atmos., 110, D18104, doi:10.1029/2005JD005776, 2005.

He, C. L., Li, Q. B., Liou, K. N., Takano, Y., Gu, Y., Qi, L., Mao, Y. H., and Leung, L. R.: Black carbon radiative forcing over the Tibetan Plateau, Geophys. Res. Lett., 41, 7806–7813, 2014.

Hegg, D. A., Warren, S. G., Grenfell, T. C., Sarah J Doherty, and Clarke, A. D.: Sources of light-absorbing aerosol in arctic snow and their seasonal variation, Atmos. Chem. Phys., 10, 10923–10938, doi:10.5194/acp-10-10923-2010, 2010.

Holben, B. N., Eck, T. F., and Fraser, R. S.: Temporal and Spatial Variability of Aerosol Optical Depth in the Sahel Region in Relation to Vegetation Remote-Sensing, Int. J. Remote Sens., 12, 1147–1163, 1991.

Holben, B. N., Tanre, D., Smirnov, A., Eck, T. F., Slutsker, I., Abuhassan, N., Newcomb, W. W., Schafer, J. S., Chatenet, B., Lavenu, F., Kaufman, Y. J., Castle, J. V., Setzer, A., Markham, B., Clark, D., Frouin, R., Halthore, R., Karneli, A., O'Neill, N. T., Pietras, C., Pinker, R. T., Voss, K., and Zibordi, G.: An emerging ground-based aerosol climatology: Aerosol optical depth from AERONET, J. Geophys. Res.-Atmos., 106, 12067–12097, 2001.

Holben, B. N., Eck, T. F., Slutsker, I., Smirnov, A., Sinyuk, A., Schafer, J., Giles, D., and Dubovik, O.: AERONET's Version 2.0 quality assurance criteria, Remote Sensing of the Atmosphere and Clouds, 6408, 64080Q, doi:10.1117/12.706524, 2006.

Hsu, S. C., Liu, S. C., Huang, Y. T., Chou, C. C. K., Lung, S. C. C., Liu, T. H., Tu, J. Y., and Tsai, F. J.: Long-range southeastward transport of Asian biosmoke pollution: Signature detected by aerosol potassium in Northern Taiwan, J. Geophys. Res.-Atmos., 114, D14301, doi:10.1029/2009JD011725, 2009.

Huang, J. P., Minnis, P., Chen, B., Huang, Z. W., Liu, Z. Y., Zhao, Q. Y., Yi, Y. H., and Ayers, J. K.: Long-range transport and vertical structure of Asian dust from CALIPSO and surface measurements during PACDEX, J. Geophys. Res.-Atmos., 113, D23212, doi:10.1029/2008JD010620, 2008.

Huang, J. P., Fu, Q. A., Zhang, W., Wang, X., Zhang, R. D., Ye, H., and Warren, S. G.: Dust and Black Carbon in Seasonal Snow across Northern China, B. Am. Meteorol. Soc., 92, 175–181, 2011.

Huang, J. P., Liu, J. J., Chen, B., and Nasiri, S. L.: Detection of anthropogenic dust using CALIPSO lidar measurements, Atmos. Chem. Phys., 15, 11653–11665, doi:10.5194/acp-15-11653-2015, 2015.

Ichoku, C., Chu, D. A., Mattoo, S., Kaufman, Y. J., Remer, L. A., Tanre, D., Slutsker, I., and Holben, B. N.: A spatio-temporal approach for global validation and analysis of MODIS aerosol products, Geophys. Res. Lett., 29, 1616, doi:10.1029/2001GL013206, 2002a.

Ichoku, C., Levy, R., Kaufman, Y. J., Remer, L. A., Li, R. R., Martins, V. J., Holben, B. N., Abuhassan, N., Slutsker, I., Eck, T. F., and Pietras, C.: Analysis of the performance characteristics of the five-channel Microtops II Sun photometer for measuring aerosol optical thickness and precipitable water vapor, J. Geophys. Res.-Atmos., 107, 4179, doi:10.1029/2001JD001302, 2002b.

IPCC: Climate Change 2013: The Physical Science Basis. Contribution of Working Group I to the Fifth Assessment Report of the Intergovernmental Panel on Climate Change, edited by: Stocker, T. F., Qin, D., Plattner, G.-K., Tignor, M., Allen, S. K., Boschung, J., Nauels, A., Xia, Y., Bex, V., and Midgley, P. M., Cambridge Univ. Press, Cambridge, United Kingdom and New York, NY, USA, 2013.

Jaffe, D., Anderson, T., Covert, D., Kotchenruther, R., Trost, B., Danielson, J., Simpson, W., Berntsen, T., Karlsdottir, S., Blake, D., Harris, J., Carmichael, G., and Uno, I.: Transport of Asian air pollution to North America, Geophys. Res. Lett., 26, 711–714, 1999.

Kang, L. T., Huang, J. P., Chen, S. Y., and Wang, X.: Long-term trends of dust events over Tibetan Plateau during 1961–2010, Atmos. Environ., 125, 188–198, 2016.

Kaufman, Y. J., Tanre, D., Gordon, H. R., Nakajima, T., Lenoble, J., Frouin, R., Grassl, H., Herman, B. M., King, M. D., and Teillet, P. M.: Passive remote sensing of tropospheric aerosol and atmospheric correction for the aerosol effect, J. Geophys. Res.-Atmos., 102, 16815–16830, 1997.

Kokhanovsky, A. A. and Zege, E. P.: Scattering optics of snow, Appl. Optics, 43, 1589–1602, 2004.

Lafon, S., Sokolik, I. N., Rajot, J. L., Caquineau, S., and Gaudichet, A.: Characterization of iron oxides in mineral dust aerosols: Implications for light absorption, J. Geophys. Res.-Atmos., 111, D21207, doi:10.1029/2005JD007016, 2006.

Li, Z., Lau, W. K.-M., Ramanathan, V., Wu, G., Ding, Y., Manoj, M. G., Liu, J., Qian, Y., Li, J., Zhou, T., Fan, J., Rosenfeld, D., Ming, Y., Wang, Y., Huang, J., Wang, B., Xu, X., Lee, S.-S., Cribb, M., Zhang, F., Yang, X., Zhao, C., Takemura, T., Wang, K., Xia, X., Yin, Y., Zhang, H., Guo, J., Zhai, P. M., Sugimoto, N., Babu, S. S., and Brasseur, G. P.: Aerosol and monsoon climate interactions over Asia, Rev. Geophys., 54, 866–929, doi:10.1002/2015RG000500, 2016.

Light, B., Eicken, H., Maykut, G. A., and Grenfell, T. C.: The effect of included particulates on the spectral albedo of sea ice, J. Geophys. Res.-Ocean., 103, 27739–27752, 1998.

Liou, K. N., Takano, Y., and Yang, P.: Light absorption and scattering by aggregates: Application to black carbon and snow grains, J. Quant. Spectrosc. Ra., 112, 1581–1594, 2011.

Liou, K. N., Takano, Y., He, C., Yang, P., Leung, L. R., Gu, Y., and Lee, W. L.: Stochastic parameterization for light absorption by internally mixed BC/dust in snow grains for application to climate models, J. Geophys. Res.-Atmos., 119, 7616–7632, 2014.

Lorenz, K., Preston, C. M., and Kandeler, E.: Soil organic matter in urban soils: Estimation of elemental carbon by thermal oxidation and characterization of organic matter by solid-state C-13 nuclear magnetic resonance (NMR) spectroscopy, Geoderma, 130, 312–323, 2006.

Loveland, T. R. and Belward, A. S.: The IGBP-DIS global 1 km land cover data set, DISCover: first results, Int. J. Remote Sens., 18, 3291–3295, 1997.

McConnell, J. R., Edwards, R., Kok, G. L., Flanner, M. G., Zender, C. S., Saltzman, E. S., Banta, J. R., Pasteris, D. R., Carter, M. M., and Kahl, J. D. W.: 20th-century industrial black carbon emissions altered arctic climate forcing, Science, 317, 1381–1384, 2007.

More, S., Kumar, P. P., Gupta, P., Devara, P. C. S., and Aher, G. R.: Comparison of Aerosol Products Retrieved from AERONET, MICROTOPS and MODIS over a Tropical Urban City, Pune, India, Aerosol Air Qual. Res., 13, 107–121, 2013.

Morys, M., Mims, F. M., Hagerup, S., Anderson, S. E., Baker, A., Kia, J., and Walkup, T.: Design, calibration, and performance of MICROTOPS II handheld ozone monitor and Sun photometer, J. Geophys. Res.-Atmos., 106, 14573–14582, 2001.

Motoyoshi, H., Aoki, T., Hori, M., Abe, O., and Mochizuki, S.: Possible effect of anthropogenic aerosol deposition on snow albedo reduction at Shinjo, Japan, J. Meteorol. Soc. Jpn., 83A, 137–148, 2005.

Ofosu, F. G., Hopke, P. K., Aboh, I. J. K., and Bamford, S. A.: Characterization of fine particulate sources at Ashaiman in Greater Accra, Ghana, Atmos. Pollut. Res., 3, 301–310, 2012.

Painter, T. H., Barrett, A. P., Landry, C. C., Neff, J. C., Cassidy, M. P., Lawrence, C. R., McBride, K. E., and Farmer, G. L.: Impact of disturbed desert soils on duration of mountain snow cover, Geophys. Res. Lett., 34, L12502, doi:10.1029/2007GL030284, 2007.

Painter, T. H., Deems, J. S., Belnap, J., Hamlet, A. F., Landry, C. C., and Udall, B.: Response of Colorado River runoff to dust radiative forcing in snow, P. Natl. Acad. Sci. USA, 107, 17125–17130, 2010.

Painter, T. H., Bryant, A. C., and Skiles, S. M.: Radiative forcing by light absorbing impurities in snow from MODIS surface reflectance data, Geophys. Res. Lett., 39, L17502, doi:10.1029/2012GL052457, 2012.

Painter, T. H., Seidel, F. C., Bryant, A. C., Skiles, S. M., and Rittger, K.: Imaging spectroscopy of albedo and radiative forcing by light-absorbing impurities in mountain snow, J. Geophys. Res.-Atmos., 118, 9511–9523, 2013.

Pedersen, C. A., Gallet, J. C., Strom, J., Gerland, S., Hudson, S. R., Forsstrom, S., Isaksson, E., and Berntsen, T. K.: In situ observations of black carbon in snow and the corresponding spectral surface albedo reduction, J. Geophys. Res.-Atmos., 120, 1476–1489, 2015.

Pio, C. A., Legrand, M., Oliveira, T., Afonso, J., Santos, C., Caseiro, A., Fialho, P., Barata, F., Puxbaum, H., Sanchez-Ochoa, A., Kasper-Giebl, A., Gelencser, A., Preunkert, S., and Schock, M.: Climatology of aerosol composition (organic versus inorganic) at nonurban sites on a west-east transect across Europe, J. Geophys. Res.-Atmos., 112, D23S02, doi:10.1029/2006JD008038, 2007.

Porter, J. N., Miller, M., Pietras, C., and Motell, C.: Ship-based sun photometer measurements using Microtops sun photometers, J. Atmos. Ocean. Tech., 18, 765–774, 2001.

Pu, W., Wang, X., Zhang, X. Y., Ren, Y., Shi, J. S., Bi, J. R., and Zhang, B. D.: Size Distribution and Optical Properties of Particulate Matter (PM_{10}) and Black Carbon (BC) during Dust Storms and Local Air Pollution Events across a Loess Plateau Site, Aerosol Air Qual. Res., 15, 2212–2224, 2015.

Qian, Y., Wang, H. L., Zhang, R. D., Flanner, M. G., and Rasch, P. J.: A sensitivity study on modeling black carbon in snow and its radiative forcing over the Arctic and Northern China, Environ. Res. Lett., 9, 064001, doi:10.1088/1748-9326/9/6/064001, 2014.

Remer, L. A., Tanre, D., Kaufman, Y. J., Ichoku, C., Mattoo, S., Levy, R., Chu, D. A., Holben, B., Dubovik, O., Smirnov, A., Martins, J. V., Li, R. R., and Ahmad, Z.: Validation of MODIS aerosol retrieval over ocean, Geophys. Res. Lett., 29, 1618, doi:10.1029/2001GL013204, 2002.

Routray, A., Mohanty, U. C., Osuri, K. K., and Prasad, S. K.: Improvement of Monsoon Depressions Forecast with Assimilation of Indian DWR Data Using WRF-3DVAR Analysis System, Pure Appl. Geophys., 170, 2329–2350, 2013.

Rozenberg, G.: Optical characteristics of thick weakly absorbing scattering layers, Dokl. Akad. Nauk SSSR, 145, 775–777, 1962.

Smith, T. M., Gao, J. D., Calhoun, K. M., Stensrud, D. J., Manross, K. L., Ortega, K. L., Fu, C. H., Kingfield, D. M., Elmore, K. L., Lakshmanan, V., and Riedel, C.: Examination of a Real-Time 3DVAR Analysis System in the Hazardous Weather Testbed, Weather Forecast., 29, 63–77, 2014.

Sokolik, I. N. and Toon, O. B.: Incorporation of mineralogical composition into models of the radiative properties of mineral aerosol from UV to IR wavelengths, J. Geophys. Res.-Atmos., 104, 9423–9444, 1999.

Srivastava, K. and Bhardwaj, R.: Analysis and very short range forecast of cyclone "AILA" with radar data assimilation with rapid intermittent cycle using ARPS 3DVAR and cloud analysis techniques, Meteorol. Atmos. Phys., 124, 97–111, 2014.

Toon, O. B., Mckay, C. P., Ackerman, T. P., and Santhanam, K.: Rapid Calculation of Radiative Heating Rates and Photodissociation Rates in Inhomoge'neous Multiple-Scattering Atmospheres, J. Geophys. Res.-Atmos., 94, 16287–16301, 1989.

Wang, M., Xu, B. Q., Zhao, H. B., Cao, J. J., Joswiak, D., Wu, G. J., and Lin, S. B.: The Influence of Dust on Quantitative Measurements of Black Carbon in Ice and Snow when Using a Thermal Optical Method, Aerosol Sci. Tech., 46, 60–69, 2012.

Wang, P., Che, H. Z., Zhang, X. C., Song, Q. L., Wang, Y. Q., Zhang, Z. H., Dai, X., and Yu, D. J.: Aerosol optical properties of regional background atmosphere in Northeast China, Atmos. Environ., 44, 4404–4412, 2010.

Wang, X., Huang, J. P., Ji, M. X., and Higuchi, K.: Variability of East Asia dust events and their long-term trend, Atmos. Environ., 42, 3156–3165, 2008.

Wang, X., Huang, J. P., Zhang, R. D., Chen, B., and Bi, J. R.: Surface measurements of aerosol properties over northwest China during ARM China 2008 deployment, J. Geophys. Res.-Atmos., 115, D00k27, doi:10.1029/2009JD013467, 2010.

Wang, X., Doherty, S. J., and Huang, J. P.: Black carbon and other light-absorbing impurities in snow across Northern China, J. Geophys. Res.-Atmos., 118, 1471–1492, 2013a.

Wang, X. G., Parrish, D., Kleist, D., and Whitaker, J.: GSI 3DVar-Based Ensemble-Variational Hybrid Data Assimilation for NCEP Global Forecast System: Single-Resolution Experiments, Mon. Weather. Rev., 141, 4098–4117, 2013b.

Wang, X., Xu, B. Q., and Ming, J.: An Overview of the Studies on Black Carbon and Mineral Dust Deposition in Snow and Ice Cores in East Asia, J. Meteorol. Res.-Prc., 28, 354–370, 2014.

Wang, X., Pu, W., Zhang, X. Y., Ren, Y., and Huang, J. P.: Water-soluble ions and trace elements in surface snow and their potential source regions across northeastern China, Atmos. Environ., 114, 57–65, 2015.

Warren, S. G.: Optical-Properties of Snow, Rev. Geophys., 20, 67–89, 1982.

Warren, S. G. and Wiscombe, W. J.: A Model for the Spectral Albedo of Snow .2. Snow Containing Atmospheric Aerosols, J. Atmos. Sci., 37, 2734–2745, 1980.

Warren, S. G. and Wiscombe, W. J.: Dirty Snow after Nuclear-War, Nature, 313, 467–470, 1985.

Wright, P., Bergin, M., Dibb, J., Lefer, B., Domine, F., Carman, T., Carmagnola, C., Dumont, M., Courville, Z., Schaaf, C., and Wang, Z. S.: Comparing MODIS daily snow albedo to spectral albedo field measurements in Central Greenland, Remote Sens. Environ., 140, 118–129, 2014.

Wuttke, S., Seckmeyer, G., Bernhard, G., Ehramjian, J., McKenzie, R., Johnston, P., and O'Neill, M.: New spectroradiometers complying with the NDSC standards, J. Atmos. Ocean. Tech., 23, 241–251, 2006a.

Wuttke, S., Seckmeyer, G., and König-Langlo, G.: Measurements of spectral snow albedo at Neumayer, Antarctica, Ann. Geophys., 24, 7–21, doi:10.5194/angeo-24-7-2006, 2006b.

Xia, X. A., Chen, H. B., Wang, P. C., Zong, X. M., Qiu, J. H., and Gouloub, P.: Aerosol properties and their spatial and temporal variations over North China in spring 2001, Tellus B, 57, 28–39, 2005.

Xia, X. G., Li, Z. Q., Holben, B., Wang, P., Eck, T., Chen, H. B., Cribb, M., and Zhao, Y. X.: Aerosol optical properties and radiative effects in the Yangtze Delta region of China, J. Geophys. Res.-Atmos., 112, D22s12, doi:10.1029/2007JD008859, 2007.

Xu, B. Q., Cao, J. J., Hansen, J., Yao, T. D., Joswia, D. R., Wang, N. L., Wu, G. J., Wang, M., Zhao, H. B., Yang, W., Liu, X. Q., and He, J. Q.: Black soot and the survival of Tibetan glaciers, P. Natl. Acad. Sci. USA, 106, 22114–22118, 2009.

Xu, B. Q., Cao, J. J., Joswiak, D. R., Liu, X. Q., Zhao, H. B., and He, J. Q.: Post-depositional enrichment of black soot in snowpack and accelerated melting of Tibetan glaciers, Environ. Res. Lett., 7, 014022, doi:10.1088/1748-9326/7/1/014022, 2012.

Yasunari, T. J., Bonasoni, P., Laj, P., Fujita, K., Vuillermoz, E., Marinoni, A., Cristofanelli, P., Duchi, R., Tartari, G., and Lau, K.-M.: Estimated impact of black carbon deposition during pre-monsoon season from Nepal Climate Observatory – Pyramid data and snow albedo changes over Himalayan glaciers, Atmos. Chem. Phys., 10, 6603–6615, doi:10.5194/acp-10-6603-2010, 2010.

Yasunari, T. J., Koster, R. D., Lau, W. K. M., and Kim, K. M.: Impact of snow darkening via dust, black carbon, and organic carbon on boreal spring climate in the Earth system, J. Geophys. Res.-Atmos., 120, 5485–5503, 2015.

Ye, H., Zhang, R. D., Shi, J. S., Huang, J. P., Warren, S. G., and Fu, Q.: Black carbon in seasonal snow across northern Xinjiang in northwestern China, Environ. Res. Lett., 7, 044002, doi:10.1088/1748-9326/7/4/044002, 2012.

Yesubabu, V., Srinivas, C. V., Hariprasad, K. B. R. R., and Baskaran, R.: A Study on the Impact of Observation Assimilation on the Numerical Simulation of Tropical Cyclones JAL and THANE Using 3DVAR, Pure Appl. Geophys., 171, 2023–2042, 2014.

Zawadzka, O., Makuch, P., Markowicz, K. M., Zielinski, T., Petelski, T., Ulevicius, V., Strzalkowska, A., Rozwadowska, A., and Gutowska, D.: Studies of aerosol optical depth with the use of Microtops II sun photometers and MODIS detectors in coastal areas of the Baltic Sea, Acta Geophys., 62, 400–422, 2014.

Zege, Ė. P., Ivanov, A. P., and Katsev, I. L.: Image transfer through a scattering medium, Springer Verlag, New York, 1991.

Zhang, R., Hegg, D. A., Huang, J., and Fu, Q.: Source attribution of insoluble light-absorbing particles in seasonal snow across northern China, Atmos. Chem. Phys., 13, 6091–6099, doi:10.5194/acp-13-6091-2013, 2013a.

Zhang, R., Jing, J., Tao, J., Hsu, S.-C., Wang, G., Cao, J., Lee, C. S. L., Zhu, L., Chen, Z., Zhao, Y., and Shen, Z.: Chemical characterization and source apportionment of $PM_{2.5}$ in Beijing: seasonal perspective, Atmos. Chem. Phys., 13, 7053–7074, doi:10.5194/acp-13-7053-2013, 2013b.

Zhang, X. L., Wu, G. J., Kokhanovsky, A., Yao, T. D., and Tong D.: Spectral albedo parameterization for dirty snow with considering mirco-physicochemical properties of impurities – Part I: Theory and preliminary evaluation, in preparation, 2017.

Zhang, X. Y., Gong, S. L., Shen, Z. X., Mei, F. M., Xi, X. X., Liu, L. C., Zhou, Z. J., Wang, D., Wang, Y. Q., and Cheng, Y.: Characterization of soil dust aerosol in China and its transport and distribution during 2001 ACE-Asia: 1. Network observations, J. Geophys. Res.-Atmos., 108, 4261, doi:10.1029/2002JD002632, 2003.

Zhao, C., Hu, Z., Qian, Y., Ruby Leung, L., Huang, J., Huang, M., Jin, J., Flanner, M. G., Zhang, R., Wang, H., Yan, H., Lu, Z., and Streets, D. G.: Simulating black carbon and dust and their radiative forcing in seasonal snow: a case study over North China with field campaign measurements, Atmos. Chem. Phys., 14, 11475–11491, doi:10.5194/acp-14-11475-2014, 2014.